

2D materials for quantum information science

Xiaolong Liu¹ and Mark C. Hersam^{1,2,3,4*}

Abstract | The transformation of digital computers from bulky machines to portable systems has been enabled by new materials and advanced processing technologies that allow ultrahigh integration of solid-state electronic switching devices. As this conventional scaling pathway has approached atomic-scale dimensions, the constituent nanomaterials (such as SiO₂ gate dielectrics, poly-Si floating gates and Co–Cr–Pt ferromagnetic alloys) increasingly possess properties that are dominated by quantum physics. In parallel, quantum information science has emerged as an alternative to conventional transistor technology, promising new paradigms in computation, communication and sensing. The convergence between quantum materials properties and prototype quantum devices is especially apparent in the field of 2D materials, which offer a broad range of materials properties, high flexibility in fabrication pathways and the ability to form artificial states of quantum matter. In this Review, we discuss the quantum properties and potential of 2D materials as solid-state platforms for quantum-dot qubits, single-photon emitters, superconducting qubits and topological quantum computing elements. By focusing on the interplay between quantum physics and materials science, we identify key opportunities and challenges for the use of 2D materials in the field of quantum information science.

In 1981, Richard Feynman famously proclaimed¹ “Nature isn’t classical, dammit, and if you want to make a simulation of nature, you’d better make it quantum mechanical.” Over the subsequent four decades, growing efforts have been devoted to the development of quantum computation, ultimately culminating in recent demonstrations of rudimentary quantum computing devices by major technology companies and significant government investments around the world in quantum information sciences. Although these recent developments have led to heightened interest in quantum technologies, substantial obstacles remain before quantum computers can reach the complexity and ubiquity of conventional computers based on integrated circuit technology and achieve quantum supremacy (that is, the ability to solve a problem too complex for a classical computer).

The potential of a hypothetical quantum computer was demonstrated in 1994 by Peter Shor, when he theoretically showed how popular encryption schemes based on factorization could be cracked by a quantum algorithm (Shor’s algorithm²) more efficiently than by any classical algorithm. However, quantum computers running such quantum algorithms are non-trivial to realize. In 2000, David DiVincenzo from IBM outlined five stringent requirements for the physical implementation of a quantum computer, including the readability, reliability and scalability of qubits, as well as the ability

to initialize qubits and the realization of a universal set of quantum gates³. Following early work using nuclear magnetic resonance⁴, Shor’s algorithm was implemented in 2016 within an ion-trap quantum computer with seven effective qubits⁵. However, large-scale integration of ion-trap qubits remains a substantial challenge that hinders the scalability of this type of quantum computer. By contrast, drawing inspiration from the success of solid-state devices in driving the microelectronics revolution, the development of quantum materials that can enable solid-state quantum computing is viewed to be foundational to the anticipated quantum revolution. Among possible quantum materials, 2D materials — defined here as thin layers that display physical properties different from those of their bulk counterparts — are of particular interest, owing to the many quantum phenomena that emerge in the atomically thin limit (such as massless Dirac fermions⁶, anyons⁷ and the quantum spin Hall effect⁸). In addition, the interlayer van der Waals bonding in 2D materials provides significant versatility in growth, functionalization and heterostructure integration, which facilitate scalable processing into complex systems⁹. In an effort to assess the status and promise of 2D materials for quantum technologies, we present here a comprehensive Review of recent research on 2D materials and heterostructures in the context of quantum information

¹Applied Physics Graduate Program, Northwestern University, Evanston, IL, USA.

²Department of Materials Science and Engineering, Northwestern University, Evanston, IL, USA.

³Department of Chemistry, Northwestern University, Evanston, IL, USA.

⁴Department of Electrical and Computer Engineering, Northwestern University, Evanston, IL, USA.

*e-mail: m-hersam@northwestern.edu

<https://doi.org/10.1038/s41578-019-0136-x>

science, focusing primarily on key challenges and opportunities from a materials perspective.

Quantum-dot qubits

Quantum computation using the spin states of trapped charges in quantum dots (QDs)¹⁰ was proposed in 1998 (REF.¹¹): the idea is to tune the inter-dot coupling in a two-qubit gate by electrically gating the tunnelling barrier. This system is attractive because exchange coupling between neighbouring QDs and the ability to induce the rotation of a single spin (via spin–orbit interaction¹² or electron spin resonance, which can be electrically driven^{13,14} or magnetically controlled¹⁵) are sufficient conditions for the realization of quantum gates for a universal quantum computer¹¹. Towards this end, various classes of QDs have been explored, including QDs based on GaAs, InGaAs, Si and nanowires, in which single-electron, double-electron and triple-electron trapping, entanglement-state preparation and state readout using both current and charge sensing have been demonstrated^{10,16–18}. In addition to spin qubits that exploit the spin degree of freedom of trapped charges, charge qubits^{19,20}, spin–orbit qubits (in which spin–orbit wave functions are used for qubit manipulation)²¹ and resonant exchange qubits (based on the spin-exchange interaction in triple QDs)^{17,18} have been demonstrated in conventional semiconductor QD devices, as outlined in several review articles^{10,16}. The promise of semiconductor QD qubits for scalable quantum circuits and long-distance quantum communication has been corroborated by recent successes in strong and coherent coupling of QD qubits with microwave photons^{18,22–24}. Because spin decoherence is typically a result of spin–orbit coupling and hyperfine interactions with nuclear spins²⁵, graphene is predicted to have exceptionally long spin decoherence times²⁶, owing to its weak spin–orbit coupling²⁷ and low natural abundance of the carbon isotope carrying a net nuclear magnetic moment, ¹³C (~1%). Moreover, graphene has been shown²⁸ to possess an electron spin g-factor of ~2, which is approximately a factor of 5 greater than that of GaAs QDs²⁹. In this section, we review experimental progress on the realization of qubits based on QDs in graphene and 2D semiconductors, such as transition-metal dichalcogenides (TMDCs).

Graphene quantum dots. When the charging energy ($Q^2/2C$, where Q is the electric charge and C is the self-capacitance) of an isolated island is non-negligible (that is, $Q^2/2C > k_B T$, where k_B is the Boltzmann constant and T is the temperature), the charge state of the island can significantly influence its charge-transport properties. In particular, when an island is electrically coupled to charge reservoirs via high-impedance barriers (such as tunnelling connections), the occupation of the island with a single electron can impede further current flow due to Coulomb repulsion (a phenomenon known as Coulomb blockade). Devices based on this principle are often referred to as single-electron transistors. The island can be metallic (for example, Al) with a quasi-continuous excitation spectrum, or a QD with a large Fermi wavelength (for example, a semiconductor QD)

and a discrete excitation spectrum. Individual electrons can pass through the QD when the electrochemical potential in the dot is tuned into the bias window (FIG. 1a) via gating. These individual charge-transport events appear as periodic peaks in plots of the conductance as a function of the single-electron transistor gate voltage³⁰ (FIG. 1b). Because the charging energy of QDs can vary from a few millielectron volts to tens of millielectron volts, depending on the dot size, Coulomb-blockade measurements are typically performed at cryogenic temperatures, although room-temperature observations have also been reported^{31,32}. As the dimensions of the QD are reduced, quantum confinement effects play an increasingly important role, altering the spacing of the discrete-energy levels.

Coulomb-blockade behaviour was observed in early experiments on lithographically defined graphene QD devices fabricated on SiO₂ surfaces³³. Graphene QDs with a size of ~100 nm show well-defined and periodic Coulomb diamonds, but variations in peak spacing and diamond sizes appear as the QD size is reduced. Graphene QDs below 30 nm in size exhibit random peak spacings that can be understood in terms of chaotic Dirac billiards³⁴. A convenient strategy for creating barriers to separate QDs from contact electrodes is to lithographically define narrow constrictions in graphene, which creates a transport gap³⁵, due to quantum confinement^{36,37}. As a result of the relatively weak electrostatic screening in graphene, the doping level and polarity in these constrictions and the QD can be tuned by local gates and a plunger gate, respectively, while the overall potential of the device is further controlled by a universal back gate^{36,38} (FIG. 1c). This ability to tune the geometry and coupling in graphene QDs has enabled significant advances in the understanding of the orbital and spin states for potential qubit applications.

Landau quantization can be imposed on graphene QDs by applying an out-of-plane magnetic field. The zeroth Landau level for massless Dirac fermions in monolayer graphene uniquely sits at the charge-neutral point and is independent of magnetic field strength (the energy of the n th Landau level is $E_n = \text{sgn}(n) \sqrt{2e\hbar v_F^2 |n|} B$, where \hbar is the reduced Planck constant, v_F is the Fermi velocity and B is the magnetic field). Thus, the Dirac point in graphene QDs can be determined by measuring the electron–hole crossover point³⁷ (FIG. 1d). Also, by monitoring the evolution of Coulomb resonance peaks while changing the strength of an in-plane magnetic field, electrons filling the same orbital state but with opposite spin orientations can be identified, thus revealing the spin-filling sequence in graphene QDs²⁸.

Building upon the successful observation of excited states in graphene QDs (the increased conductance along the edges of Coulomb diamonds)^{39,40}, pulsed-gate, transient-current spectroscopy has been used to assess the relaxation dynamics of excited states in a graphene QD qubit³⁸. The measurements established a lower bound of 60–100 ns for the relaxation time, which is likely limited by electron–phonon coupling. However, if the relaxation occurs concurrently with spin flipping, the decoherence time can be significantly enhanced⁴¹. Improving the homogeneity of the graphene and

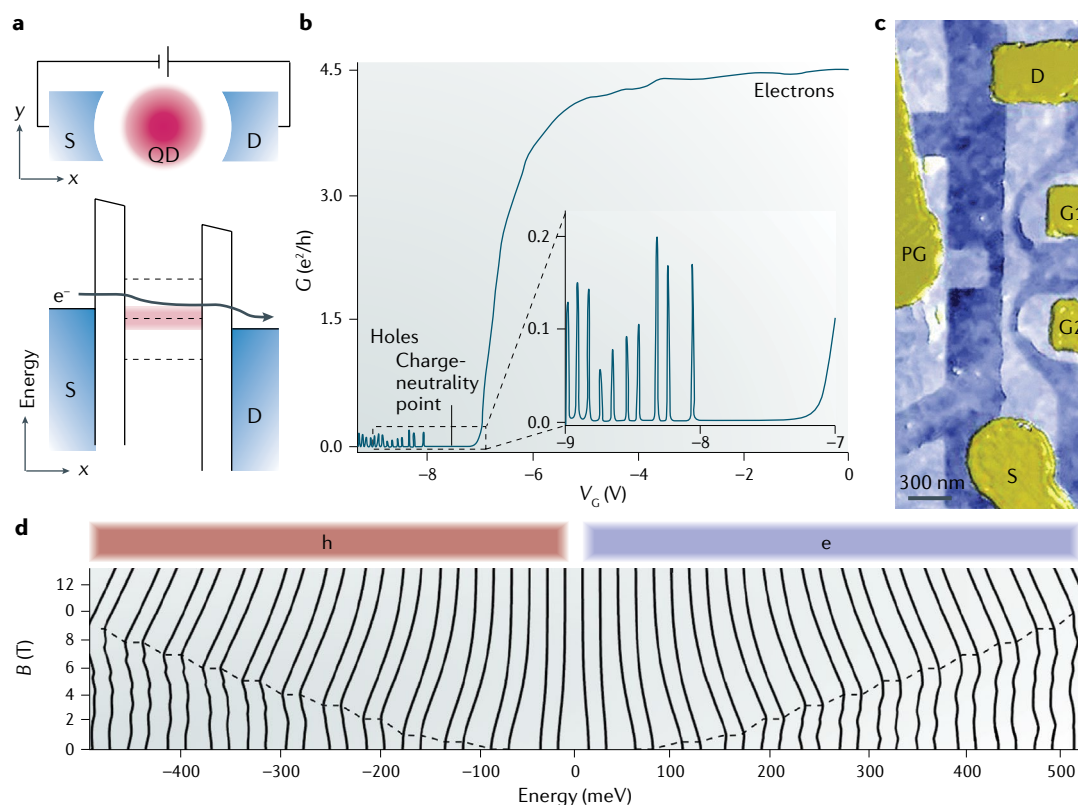


Fig. 1 | Graphene single-quantum-dot devices. **a** | Schematic representation of a quantum dot (QD) connected to source (S) and drain (D) reservoirs via tunnelling connections (top). When one of the energy levels (electrochemical potentials) of the QD falls within the bias window (pink-shaded region) owing to the application of a voltage, an electron (e) can tunnel in and out of the QD. The top schematic is a real-space representation, whereas the bottom schematic is an energy-level diagram taken along the x-direction of the QD device. **b** | Conductance, G , of a bilayer p-type graphene QD device as a function of gate voltage, V_G . When the gate voltage is lowered below the charge-neutrality point to tune the system into the hole (h) regime, the QD can be charged with individual holes and multiple Coulomb conductance peaks appear. **c** | Lithographically defined single QD in monolayer graphene with a plunger gate (PG), two local gates (G1, G2) tuning the tunnelling barriers and a global back gate (not shown). **d** | Calculated energy levels of a QD in monolayer graphene (Coulomb resonance lines) as a function of magnetic field; the lines bend towards the charge-neutrality point. Panel **b** is adapted from REF.³⁰, CC-BY-4.0. Panel **c** is adapted with permission from REF.³⁶, ACS. Panel **d** is adapted with permission from REF.³⁷, APS.

surrounding materials (for example, using hexagonal boron nitride, hBN, in place of SiO_2 as the substrate)⁴² can improve the quality and reliability of graphene QDs. Because the size of charge puddles is an order of magnitude larger for graphene/hBN than for graphene/ SiO_2 (REF.⁴³), the potential disorder that would break a single graphene QD into multiple QDs is mitigated, especially if the QD size is comparable to that of the charge puddles.

The imperfect edges and resulting localized edge states in lithographically defined graphene QDs lead to disorder that compromises the quality and reproducibility of quantum confined states and renders QDs disorder-dominated, even in a homogeneous dielectric environment (such as hBN encapsulation). Such QDs are thus not promising for qubit applications. To mitigate these issues, graphene QDs can be defined electrostatically through the application of gate potentials. However, the massless Dirac fermions in graphene have a unity probability of leaking through a confinement barrier if the incident angle is zero (Klein tunnelling)⁴⁴,

which makes it challenging to form true bound states in monolayer graphene^{45,46}. Therefore, for electrostatically defined QDs, Bernal-stacked (AB stacking) bilayer graphene is often employed; in this system, tighter bound states have been experimentally realized, owing to the opening of a band gap^{47,48} upon application of an out-of-plane electric field that breaks inversion symmetry⁴⁹. Although bilayer graphene generally hosts soliton-like AB–BA domain walls⁵⁰ that can act as undesirable conducting channels⁵¹, electrostatically defined bilayer graphene QDs, particularly when sandwiched between hBN layers, present clear advantages as qubit candidates over alternative graphene QD systems^{30,52,53}. For example, single-electron confinement and successive electron filling, which are essential for qubit manipulation, have been demonstrated in electrostatically defined bilayer graphene QDs after improving the pinch-off resistance by using a graphite back gate³⁰. The ground and excited states of hBN-encapsulated bilayer graphene QDs have been recently measured and found to be fundamentally different from those of GaAs-based QDs, owing to

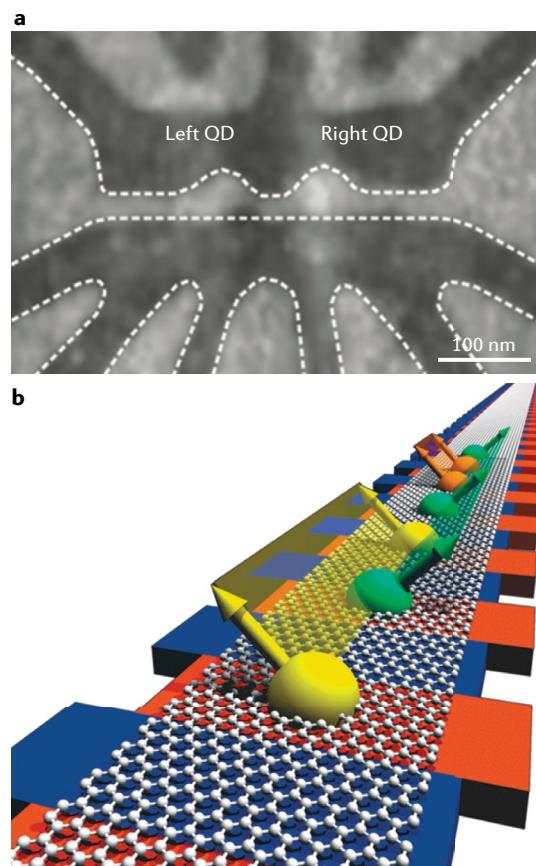


Fig. 2 | Graphene multi-quantum-dot devices.
a | Lithographically defined bilayer graphene double-quantum-dot (QD) device with gate-tunable tunnelling barriers. **b** | Spin qubits along a monolayer graphene nanoribbon with armchair edges. The QDs are tuned by the red gates and the inter-dot coupling by the blue gates. As a result of Klein tunnelling, qubits can be coupled over relatively long distances, as schematically represented by spins with the same colour. Panel **a** is adapted with permission from REF.⁵⁹, ACS. Panel **b** is reproduced with permission of Guido Burkhard, University of Konstanz, Germany.

two-fold valley and spin degeneracies⁵⁴. In monolayer graphene, quantum confinement has also been achieved through strain-induced, pseudo-magnetic fields generated by a scanning tunnelling microscopy (STM) tip⁵⁵. Moreover, the combination of electrostatic confinement from an STM tip and an out-of-plane magnetic field allows the observation of spatially varying valley splitting in QDs in graphene/hBN moiré superlattices down to the nanometre scale, providing a means to manipulate the valley degree of freedom of the QDs⁵⁶.

Coupled QDs are not only necessary for scaling up qubit circuits but can also serve as building blocks for single qubits (such as triple-QD, resonant-exchange qubits)¹⁷. In particular, multi-QD qubits allow all-electrical control at a lower control signal frequency as compared with single-QD qubits³⁷, albeit with more complicated device geometries. As a compromise, double-QD qubits (FIG. 2a) that utilize two spin states (singlet and triplet states) have emerged as promising candidates for coupled QD qubits¹¹. As for single QDs,

excited states and charge pumping for qubit readout have been reported for double-QD qubits^{40,58–60}. However, for double-QD qubits based on monolayer graphene, the orbital degeneracy in the K and K' valleys modifies the form of the exchange interaction based on Pauli exclusion, allowing electron tunnelling not only in singlet states with opposite spins but also in triplet states with parallel spins, ultimately leading to fast qubit decoherence⁶¹. Theoretically, this undesirable situation can be alleviated by breaking the valley degeneracy with an external magnetic field^{62,63}. Alternatively, monolayer graphene nanoribbons with semiconducting armchair edges are predicted to lift the valley degeneracy⁶⁴ in addition to opening a band gap that is inversely proportional to the nanoribbon width, allowing Heisenberg exchange coupling for spins in electrostatically defined, neighbouring QDs⁶⁵ (FIG. 2b). This scheme can be extended to a series of QDs electrostatically defined on a single-monolayer graphene nanoribbon⁶⁴. Similarly, nanoribbons have been electrostatically defined in hBN-encapsulated bilayer graphene with a pair of split gates. Depending on the voltage and polarity applied, up to five QDs have been defined as a result of the ambipolar nature of bilayer graphene⁵². The large number of possible device configurations makes this multi-QD system a promising platform for realizing diverse types of qubits, in addition to enabling exploration of the Kondo effect⁶⁶ and spin blockade⁶⁷, which have, thus far, not been observed in graphene QDs. Unintentional creation of graphene multiple QDs has also occurred in lithographically defined graphene nanoribbon devices due to the disorder potential and resulting quantum confinement, especially for devices on SiO₂ substrates^{35,68}, as evidenced by local resonance peaks in transport gaps and the appearance of Coulomb diamonds³⁵. Finally, superconducting microwave resonators have been used to couple remote graphene double-QD qubits^{69,70}, offering a means to entangle macroscopically separated quantum systems on a chip.

2D semiconductor quantum dots. Whereas the relatively weak spin–orbit coupling in graphene is beneficial for mitigating spin decoherence, it also implies relatively slow operation of graphene-based spin qubits. Furthermore, the band gaps in both monolayer and bilayer graphene QDs are small compared with those of conventional semiconductors. Consequently, 2D semiconductors offer enticing alternatives to graphene for the realization of QD qubits, although several material requirements must be met to realize quantized transport, including small contact resistance, ballistic transport and high carrier mobility and/or low carrier concentration, such that the Fermi wavelength is comparable to the tunnelling constriction size⁷¹.

Monolayer TMDCs⁷² have direct band gaps in the range of 1.5–2.5 eV and broken inversion symmetry⁷³. Furthermore, the spin–valley degree of freedom resulting from strong spin–orbit coupling and the large exciton-binding energies make monolayer TMDCs ideal candidates for valleytronics⁷⁴ and optoelectronics⁷⁵ applications. Whereas traditional III–V semiconductor QDs are typically grown as self-assembled QDs (such as

InGaAs islands grown on GaAs (REF.⁷⁶), lateral QDs (such as electrostatically defined QDs in GaAs/AlGaAs heterostructures⁷⁷) and nanowire QDs (such as InAs QDs defined by InP barriers along nanowires⁷⁸), TMDC QDs can be conveniently created by electrostatic gating, in both monolayer and few-layer systems. Moreover, the strong intrinsic spin–orbit coupling in TMDCs (which, owing to reduced symmetry, have a different Hamiltonian than that of III–V semiconductors⁷⁹) allows fast spin rotation, which is ideal for qubit operations. Qubits based on TMDC QDs, including spin qubits, valley qubits and hybrid spin–valley qubits based on electrostatically defined, monolayer MoS₂ QDs, have been recently theoretically explored^{79–81}. The large spin–orbit coupling in these systems leads to a splitting of the two spin-degenerate and valley-degenerate states into two Kramers pairs at zero magnetic field. The spin qubits can then be manipulated by electron spin resonance, whereas the valley qubits can be controlled with an AC electric field without affecting the spin. In addition, simultaneous flipping of the spin and valley states can be achieved in spin–valley qubits using near-range defects, AC electric fields and off-axis magnetic fields. From a theoretical perspective, these hybrid spin–valley qubits are attractive owing to their long coherence times, resulting from the requirement that decoherence processes couple to both spin and valley degrees of freedom, although physical realizations of these long coherence times are yet to be demonstrated.

Quantum-transport measurements on TMDC-based QDs are sparse, because most contact metals have large Schottky barriers to TMDCs that result in high contact resistance at low temperature. Nevertheless, through the use of zinc metal contacts with low work function and of a thermally annealed metal migration step, Coulomb blockade has been observed in MoS₂ QD devices⁸². Similarly, WS₂ (REF.⁸³) and WSe₂ (REF.⁸⁴) QDs have been demonstrated. However, the multi-layer thickness (7–10 layers) of the WS₂ and WSe₂ QDs led not only to an indirect band gap but also to small spin–orbit gaps. Recently, Coulomb blockade in QDs based on encapsulated, monolayer MoS₂ has been observed⁸⁵, which may serve as the basis for future realizations of the proposed spin, valley and hybrid spin–valley qubits. Furthermore, the combination of MoS₂, graphene and hBN in van der Waals heterostructures has enabled small Schottky barriers resulting from the use of graphene contacts and minimum disorder potential thanks to hBN encapsulation in a MoS₂ QD device⁸⁶, leading to the observation of quantized conductance and gate-defined exciton confinement. With a direct band gap of ~1.3 eV and higher mobility than that of MoS₂, few-layer InSe is another emerging 2D semiconductor that shows promise for quantum transport and electrostatically defined QDs, particularly when interfaced with graphene ohmic contacts⁷¹.

Single-photon emitters in 2D materials

Ideal qubits are identical to each other. Whereas variations exist among QDs due to their non-atomic sizes, well-defined atomic-point defects in materials hold promise for applications in quantum information

science. An early example is dopant atoms (such as P atoms) in Si (REFS^{87,88}), in which the electron and nuclear spins can be utilized for quantum computation (as in the Kane quantum computer⁸⁷). However, the scalability of this qubit system remains at the proposal stage⁸⁹ and the need for isotopically pure ²⁸Si is a non-trivial engineering challenge. By contrast, owing to their atomically thin nature, surface functionalization of 2D materials⁹ provides an alternative route towards defect-based spin qubits, in which the vertical uncertainty of donor positions is effectively eliminated. Schemes along these lines have been proposed⁹⁰ but not yet realized experimentally.

Beyond spin states, the desirable optical properties of point defects originating from deep in-gap states^{91–93} and defect-bound excitons^{94,95} (FIG. 3a) can potentially be exploited for quantum communication applications due to the low transmission loss of photons, particularly at near-infrared telecommunications wavelengths. In addition, photons generally have weak interactions with the environment and, thus, long coherence times. Photonic qubit states⁹⁶ (such as the polarization state, Fock state and time-bin) are also relatively straightforward to manipulate with standard optical components. Robust, bright and indistinguishable single-photon emitters (SPEs) are essential for creating photonic qubits for efficient quantum communication. In a distributed, quantum network, photonic qubits could act as interlinks that entangle distant qubit nodes (such as spin qubits). The single-photon nature of the communication implies that any interception of the information encoded would be noticed, ensuring secure communication. Moreover, SPEs are a key ingredient in photonic quantum computing, in which the large bandwidth of photons allows high-speed operation. As such, a number of materials hosting SPEs have been explored. For example, the nitrogen-vacancy (NV) colour centre in diamond is an attractive system⁹⁷, both as a spin qubit and as a SPE due to its long decoherence time, reaching one second at room temperature⁹⁸, and its addressability via optical, electrical and magnetic means. NV centres in diamond have been utilized as quantum sensors owing to the high sensitivity of their spin state to environmental conditions (for example, for temperature sensing⁹⁹), and defects that are localized near or at the surface of the host material are likely to provide improved sensitivity and accessibility. However, despite progress in the growth of diamond thin films and nanowires, the difficulty of integrating diamond components into devices using traditional lithographic approaches motivates the exploration of defect states in other material systems. In this section, we discuss recent work on SPEs in 2D materials^{100,101}.

Single-photon emitters in hBN. From an electronic-structure perspective, hBN is analogous to diamond, in the sense that it has a large bandgap of ~6 eV (REF.¹⁰²). Atomic defects in wide-bandgap semiconductors often occur as highly localized electronic states within the bandgap that resemble atoms and molecules (FIG. 3a). In recent years, defect states in hBN have attracted significant attention because of their single-photon emission at ambient conditions, combined with the high mechanical

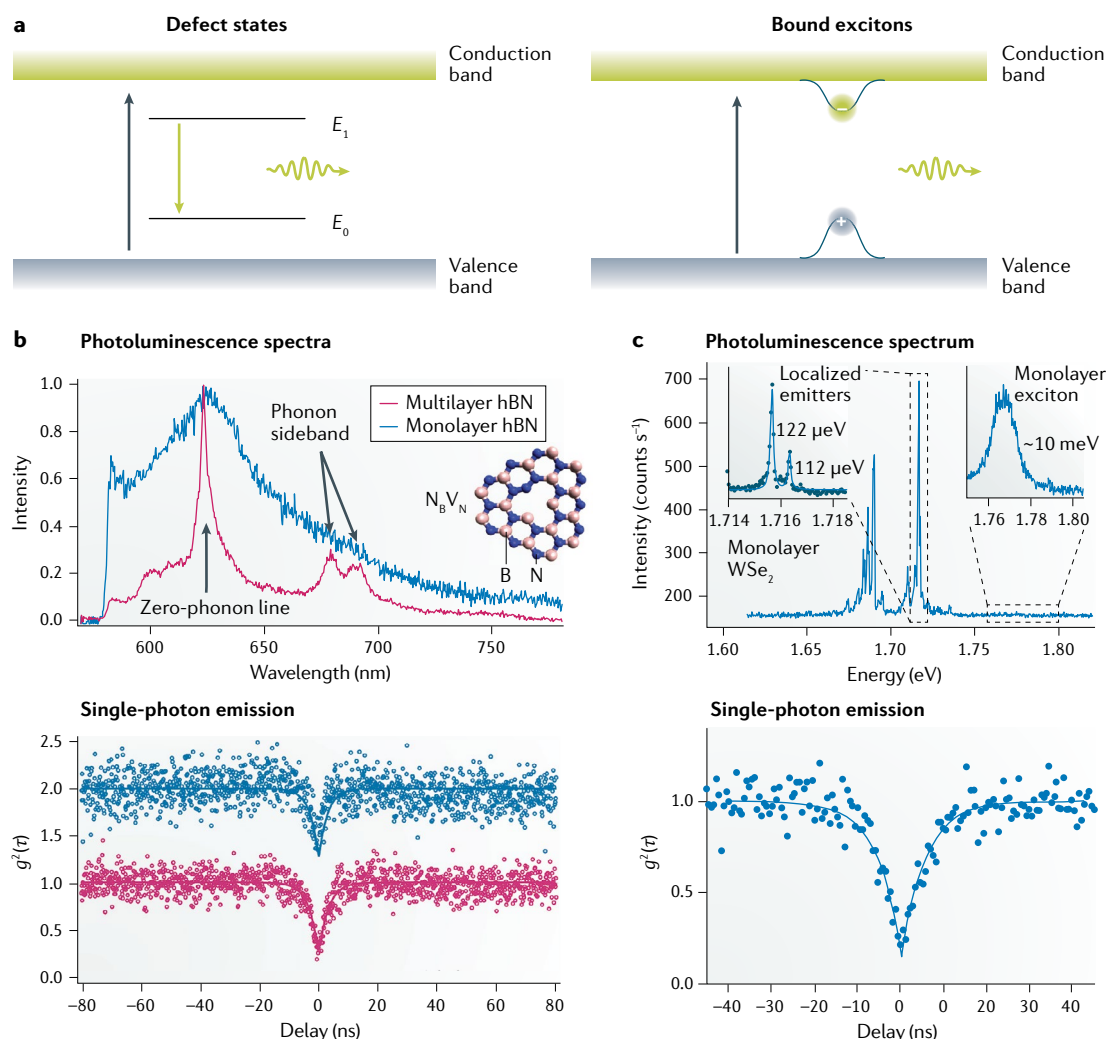


Fig. 3 | Single-photon emitters in 2D materials. **a** | Schematic representation of photoluminescence from deep in-gap states (colour centres) in a wide-gap insulator (such as hexagonal boron nitride, hBN) and from bound excitons in a narrow-gap semiconductor (such as MoS₂). E_0 and E_1 are the ground state and first excited state, respectively, of the colour centre. **b** | Photoluminescence spectra and single-photon emission from monolayer and multilayer hBN (top). The inset shows the $N_B V_N$ defect structure, in which a nitrogen atom substitutes for boron, with a vacancy on the nitrogen site. The emission lines from multilayer samples are narrower than those from monolayer samples. For both types of samples, the defects act as single-photon emitters, as demonstrated by the antibunching curves (bottom). **c** | Photoluminescence (top) and single-photon emission (bottom) from monolayer WSe₂. The insets in the top panel are zoomed-in spectra of zero-phonon lines and delocalized exciton photoluminescence; the spectrum on the right is integrated for 60 s, the spectrum on the left for 1 s. Panel **b** is adapted from REF.⁹³, Springer Nature Limited. Panel **c** is adapted from REF.¹¹⁷, Springer Nature Limited.

flexibility and chemical stability of hBN and the larger Debye–Waller factor of hBN (~ 0.82)⁹³ compared with that of NV centres (~ 0.13)¹⁰³. The absorption and emission spectra of single-photon sources are characterized by a sharp zero-phonon line (ZPL, a transition between two electronic states that does not involve phonons) and a wide and weak phonon sideband (PSB, related to electronic transitions that involve phonons). The Debye–Waller factor represents the ratio of the ZPL intensity to the total emission (that is, the SPE efficiency). During continuous optical excitation and emission, blinking of SPEs is often observed due to non-radiative recombination, resulting in dark states that can last for tens of seconds before the return of emitting states¹⁰⁴. By definition,

only one photon should be emitted from a SPE at a time; thus, the typical means of determining if a source is a SPE is by measuring second-order autocorrelation functions, $g^2(\tau)$, using a Hanbury Brown and Twiss interferometry setup¹⁰⁵. The typical criterion a SPE must satisfy is that the $g^2(\tau)$ curve should have an antibunching dip smaller than 0.5 at zero delay time ($\tau=0$; bottom panels in FIG. 3b,c).

SPEs in hBN have been observed at multiple energies around 2 eV (REF.¹⁰⁶) (~ 620 nm; FIG. 3b). Experimentally, different ZPLs show similar energy shifts from the PSBs, indicative of SPEs with analogous crystallographic structures but varying dielectric environments¹⁰⁷. Although the exact atomic structures of SPEs in hBN are still a

matter of debate, leading candidates include nitrogen vacancies (V_N), boron vacancies (V_B) and anti-site complexes ($X_B V_N$), in which an atom X (X = C, N, O) substitutes for boron with a vacancy on the nitrogen site^{108,109}. The formation and activation^{93,110} of SPEs have been achieved by electron-beam irradiation and post-annealing in Ar, O₂ or H₂ (REF.¹¹⁰). Because the areal density of SPEs increases with increasing annealing temperature in both reducing and oxidizing environments, the SPE defects in this case are likely charge neutral¹¹⁰.

For most applications in quantum information sciences, SPEs need to be patterned in a deterministic fashion and have tunable emission properties. SPEs are often observed at 2D flake edges, ripples and grain boundaries, and the patterning of holes in exfoliated hBN provides some spatial control over SPE location: quasi-periodic SPEs with an areal density of $0.33 \mu\text{m}^{-2}$ have recently been demonstrated¹¹¹. Similarly¹¹², using large-area, few-layer hBN films grown by low-pressure chemical vapour deposition on Cu, Ni and Fe substrates, an areal density of SPEs reaching $0.84 \mu\text{m}^{-2}$ has been obtained. In addition to spatial distribution, many applications require control over spectral diffusion (that is, the distribution of ZPL peak positions) and ZPL linewidth. Early SPEs in few-layer hBN suffered from relatively broad spectral diffusion, up to 200 nm (REF.¹¹⁰), which has been attributed to the inhomogeneous local dielectric environment and strain variations⁹². By contrast, by passivating the hBN surface with a 2-nm-thick alumina capping layer¹⁰⁴ that minimizes mobile charges from surface-adsorbed water, the ZPL linewidth has been reduced to 45 μeV , which is much lower than the typical values of 0.4 meV (REF.¹⁰⁶) and 1.2 meV (REF.¹¹⁰). The alumina capping layer also minimizes spectral blinking and reduces spectral diffusion to 40 nm (REF.¹⁰⁴). In high-quality chemical vapour deposition hBN films, spectral diffusion has been further reduced to 10 nm for a 580-nm ZPL¹¹².

Strain engineering is another effective strategy for tuning the optical emission from 2D materials¹¹³. For example, by bending 100-nm-thick hBN layers on polycarbonate beams⁹², the SPE spectrum shows blue and red shifts under tensile and compressive strain, respectively, although the details of the shifts depend on the orientation of the strain with respect to the high-symmetry crystallographic directions of hBN⁹². The sensitivity of SPEs to strain also partially accounts for the wide spectral diffusion that is observed in many samples⁹², particularly exfoliated flakes. Recently, SPEs in a 0D allotrope of hBN composed of wrapped-up layers of hBN with diameters of 1–100 nm, known as BN nanococoons¹¹⁴, were observed to have a relatively narrow emission line variation of 39 nm (but with low areal density of $10^{-3} \mu\text{m}^{-2}$), likely originating from the rigid structure, which minimizes strain variations.

Electrical control of SPEs offers potential advantages for integrated photonic circuits. Using electrostatic gating, spectral shifts of up to 15 nm have been observed and attributed to field-assisted photodoping¹¹², in which charges are injected and trapped at defects in close proximity to SPEs. Similarly, a Stark shift of up to 5.4 nm per GV m^{-1} of electric field was observed in thick

hBN flakes (100–200 nm) sandwiched between graphene electrodes¹⁰⁹. In this case, first-principles calculations suggest the existence of out-of-plane dipole moments associated with SPEs, which are assumed to be $X_B V_N$ defects¹⁰⁹. Specifically, two symmetrically equivalent, out-of-plane displacements of X atoms are predicted to result in two out-of-plane dipoles, consistent with experimental observations¹⁰⁹.

Single-photon emitters in TMDCs. The bandgaps of TMDC monolayers are smaller than that of hBN and direct; thus, they permit efficient generation of excitons upon optical excitation. In addition to characteristic neutral and charged exciton peaks in photoluminescence spectra, sharp emission peaks 20–100 meV lower in energy are also frequently observed¹¹⁵ and attributed to excitons bound at structural imperfections¹¹⁶ (FIG. 3a). A burst of research interest in TMDC-based SPEs occurred in 2015, when multiple studies^{95,115,117,118} reported defect-localized excitons in WSe₂, that acted as SPEs at cryogenic temperatures¹¹⁹ with an areal density of $\sim 0.05 \mu\text{m}^{-2}$ (FIG. 3c). Even though monolayer WSe₂ possesses rather short exciton lifetimes (< 100 ps)¹²⁰, the excited-state lifetime of SPEs in WSe₂ reaches 1–2 ns (REFS^{95,115,117,118}), which is similar to that of SPEs in hBN. The PSB partially overlaps with the ZPLs in WSe₂, leading to asymmetric line shapes of the ZPLs¹²¹. Under zero magnetic field, the ZPLs show a spectral splitting (0.7 meV (REFS^{95,117}) to 1 meV (REF.¹¹⁵)), which evolves in a manner consistent with a Zeeman splitting when subjected to an out-of-plane magnetic field, revealing a high excitonic g-factor of 8–10 (REFS^{95,115,117,118}). The optical emission from these SPEs is strongly linearly polarized and the polarization decreases if an out-of-plane magnetic field is applied¹¹⁷. These observations suggest that SPEs originate from neutral excitons in an anisotropic confinement potential¹¹⁵, leading to linearly polarized doublets with exchange splitting, which are converted back into circularly polarized light when the Zeeman energy overcomes the electron–hole exchange interaction¹¹⁷. Beyond WSe₂, SPEs have also been demonstrated in WS₂ (REF.¹¹⁹) and MoSe₂ (REF.¹²²). Atomic-scale visualization of point defects in TMDCs has been achieved with STM^{123–126}. Although the convolution of real-space structures with electronic effects in STM imaging prevents direct assignment of defect structures, it is generally believed that chalcogen vacancies are abundant owing to their relatively low formation energies, a hypothesis supported by first-principles calculations^{127,128}. However, the exact defects responsible for trapping excitons have not yet been definitively identified.

A significant advantage of SPEs in TMDCs compared with those in hBN lies in the ability to electrically trigger single-photon emission (that is, electroluminescence). Such electrically driven single-photon emission has been achieved by vertically stacking WSe₂ or WS₂ flakes with hBN to allow electrons and holes to tunnel through the hBN layers^{119,129}. Alternatively, lateral *p-i-n* junctions defined by gates in WSe₂ have been used to electrically excite SPEs in the junction region¹²⁹. As in hBN, intentional creation of strain fields in TMDCs can be used to trap excitons into desired geometries, thereby

allowing deterministic placement of SPEs for integration with photonic circuits. In particular, funnelling of excitons into localized, artificial atoms has been realized by inducing strain in TMDC lattices^{130,131}. SPEs with near-unity efficiency have been achieved with WSe₂ monolayers placed on top of arrays of dielectric pillars^{132,133}. Using an atomic force microscopy tip¹³⁴, WSe₂ layers on top of a polymer film have also been indented to create local strain, with tip forces ranging from tens to thousands of nanoNewtons, which resulted in the deterministic placement of SPEs with nanometre-scale precision.

2D superconducting qubits

In addition to qubits based on QDs and material defects, solid-state qubits can also be realized using superconducting circuits. High-quality superconducting qubits have stringent requirements on the interfacial cleanliness between the normal and superconducting components. The prevailing aluminium oxide used in most modern superconducting qubit designs is lossy and contains a high concentration of defects¹³⁵. In light of their superlative materials properties and device fabrication flexibility, 2D materials are beginning to be considered for superconducting qubits, particularly because the stacking of 2D layers into vertical van der Waals

heterostructures in all-dry¹³⁶ or vacuum environments¹³⁷ holds promise for creating atomically clean interfaces.

Due to the unequal energy gaps between adjacent energy levels in an anharmonic oscillator, the transition between two energy levels can be addressed and utilized as a qubit. A key component in superconducting qubits¹³⁸ and quantum metrology¹³⁹ is the Josephson junction (JJ), a heterostructure of two superconductors separated by a barrier (known as a weak link¹⁴⁰) that allows the flow of supercurrent. In a JJ, phase-coherent transport of charge carriers (that is, Andreev-reflected electron-hole pairs with discrete energy states, also known as Andreev bound states, ABSs) is required in the weak link, which can be a non-superconducting metal, an insulator, vacuum or a physical constriction that locally weakens superconductivity. Different from conventional inductors, the Josephson inductance of a JJ is a non-linear function of the Josephson phase and causes anharmonicity if the JJ is combined with a capacitor to form an inductor-capacitor (LC) circuit (FIG. 4a). The ideal Josephson effect takes place in the short-junction limit, in which the effective length (L_{eff}) of the junction is smaller than the coherence length (ξ) of superconductivity¹⁴⁰. The supercurrent, $I(t)$, and voltage, $V(t)$, where t is time, across a JJ are given by $I(t) = I_c \sin(\delta\phi(t))$ and

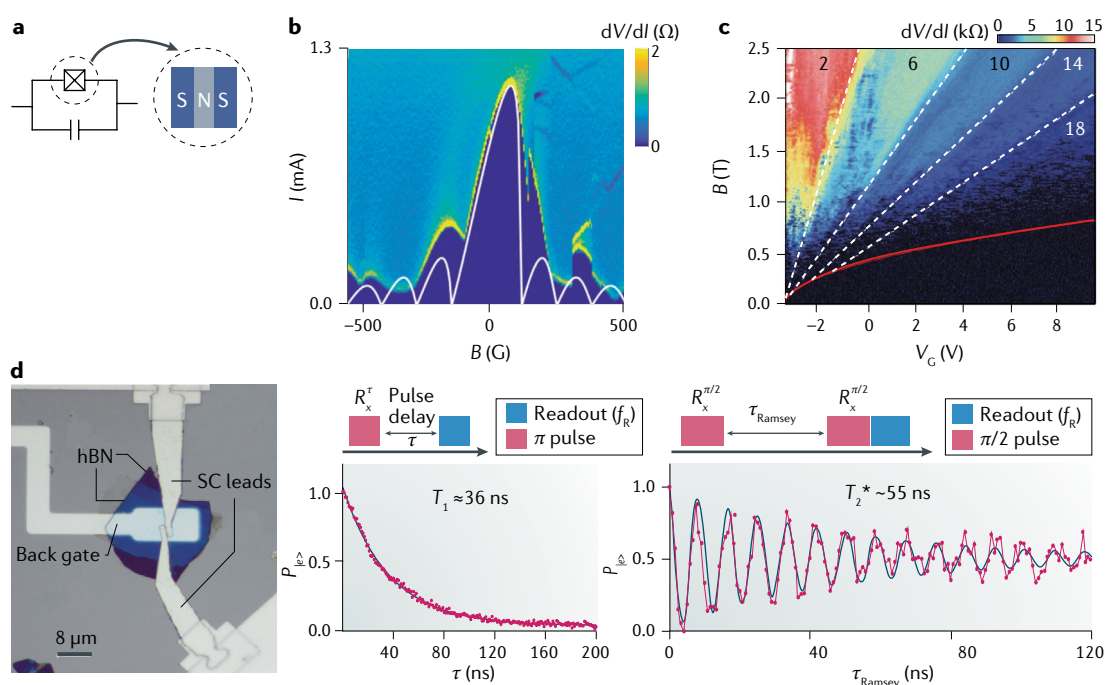


Fig. 4 | 2D superconducting qubits. **a** | Schematic illustration of a superconducting qubit and of the structure of a Josephson junction (JJ), in which a weak link (N) is sandwiched between two superconductors (S). **b** | Fraunhofer pattern from a NbSe₂/graphene/NbSe₂ JJ, in which the self-field due to the high critical current distorts the pattern. The white curve is a theoretical fit to the data. **c** | Differential resistance dV/dI as a function of gate voltage V_g and magnetic field B for a graphene-based JJ sandwiched by hexagonal boron nitride (hBN) and edge-contacted by MoRe electrodes. In addition to the quantum Hall plateaux (separated by white dashed lines), the region with zero differential resistance (where the supercurrent is observed, black region) extends beyond the classical parabolic region (marked by the red line), in which the cyclotron orbit diameter is larger than the graphene channel length. **d** | A graphene-based, gate-controlled transmon qubit (a gatemon qubit) fabricated from an encapsulated graphene JJ with Al superconducting electrodes and a shunt capacitor. The graphs show the fitting of the qubit population (left), from which the energy relaxation time T_1 is extracted, and the Ramsey fringes (right), from which the dephasing time T_2^* of the qubit is obtained. SC, superconducting. Panel **b** is adapted with permission from REF.¹⁵³, ACS. Panel **c** is adapted with permission from REF.¹⁶², AAAS. Panel **d** is reproduced from REF.¹⁶⁰, Springer Nature Limited.

$V(t) = \hbar/2e \partial\delta\varphi/\partial t$, respectively, where I_c is the junction critical current and $\delta\varphi$ is the phase difference (Josephson phase) between the order parameters in the two superconductors. If a magnetic field is applied in the direction perpendicular to the junction, a Fraunhofer pattern similar to that observed in optical diffraction develops in plots of the junction voltage or differential resistance as a function of current and magnetic field¹⁴¹. An important figure of merit of a JJ is the $I_c R_N$ product, where R_N is the normal state resistance, which is proportional to the superconducting gap (Δ) at zero temperature. In the ballistic ('clean'¹⁴⁰) regime ($l > L_{\text{eff}}$ where l is the carrier mean free path in the weak link) of a short JJ, the $I_c R_N$ product is constant and independent of geometry. In this limit, I_c and, thus, the qubit can be tuned by varying R_N (for example, via gating). By contrast, the $I_c R_N$ product becomes dependent on l when the junction is in the diffusive ('dirty'¹⁴⁰) regime ($l < L_{\text{eff}}$).

Qubits based on superconducting, anharmonic oscillators have the advantage in that they can be integrated at the wafer scale, which has led to significant commercial interest. A common implementation of a superconducting qubit is the transmon¹⁴², which is short for transmission-line shunted plasma oscillation qubit. The high ratio of Josephson energy to charging energy makes transmons relatively immune to charge noise but still sufficiently anharmonic. If the barrier material is composed of a thin-film semiconductor, the Josephson energy is further tunable by electrostatic gating, leading to gate-tunable transmons, or gatemon¹⁴³, which potentially allow microwave-free operation¹⁴⁴. In addition to the initial demonstration using InAs nanowires¹⁴³ as the barrier material, gatemon qubits have also been realized using the 2D electron gas in InAs/InGaAs heterostructures¹⁴⁵; in this system, voltage-controlled single-qubit and double-qubit operations have been demonstrated with coherence times up to 2 μs .

The massless Dirac fermions in graphene possess exceptionally high mobility, in excess of $300,000 \text{ cm}^2 \text{ V}^{-1} \text{ s}^{-1}$, in addition to ballistic transport over length scales of micrometres¹⁴⁶. Exploiting these properties, phase-coherent charge transport in graphene–superconductor hybrids was observed¹⁴⁷, establishing graphene as a weak link for JJs. Similar to the case of conventional graphene devices, early graphene-based JJs suffered from charge disorder and scattering centres in SiO_2 substrates^{147,148}, which compromised carrier mobility and mean free path, leading to diffusive rather than ballistic transport¹⁴⁹. A complicated but effective solution to this issue involves the use of suspended graphene layers with superconducting NbN contacts in a planar geometry ($I_c R_N \approx 0.33\Delta/e$)¹⁵⁰. However, a drawback of this approach is the need to use Ti adhesion layers¹⁵⁰ for NbN deposition and a Pd layer to protect Ti during NbN growth. Alternatively, ballistic transport and mitigated substrate disorder can be achieved by fabricating Al-sandwiched, vertical-graphene-based JJs ($I_c R_N \approx 2.59\Delta/e$)¹⁵¹. Whereas the use of several layers of graphene lowers I_c (REF.¹⁵¹) (as is also observed in MoS_2 JJs¹⁵²), in the absence of graphene, R_N grows by two orders of magnitude due to oxidized Ti adhesion layers, highlighting the critical role of graphene in protecting Ti and defining a sharp weak link.

The diversity of 2D materials properties provides the option of fabricating all-2D JJ heterostructures with 2D superconducting contacts, thereby eliminating the aforementioned complexities of conventional metal deposition. For example, a vertical JJ composed of multilayer NbSe_2 (bulk superconducting critical temperature T_c of $\sim 7 \text{ K}$) sandwiching a graphene layer with ballistic characteristics was realized ($I_c R_N \approx 0.5\Delta/e$)¹⁵³. Because I_c and T_c decrease as the number of layers decreases¹⁵⁴, multiple layers of NbSe_2 are necessary to maximize the operating temperature. The Josephson coupling is stronger in vertical graphene junctions with Al electrodes¹⁵¹ because the $I_c R_N$ product is higher than that for JJs with NbSe_2 electrodes, owing to a high I_c density of $16,000 \text{ A cm}^{-2}$. This large current induces a magnetic field that skews the Fraunhofer pattern, as seen by the asymmetric I_c distribution, as a function of the external magnetic field¹⁵³ (FIG. 4b). Interestingly, without graphene, the van der Waals gap formed between stacked NbSe_2 flakes can also act as a tunnelling-type weak link ($I_c R_N \approx 1.43\Delta/e$)¹⁵⁵, unlike the oxidized Ti adhesion layers discussed above¹⁵¹. Compared with the pristine van der Waals gap in NbSe_2 single crystals, the artificial gap in restacked NbSe_2 is generally larger, owing to contaminants from the transfer process, which lowers the orbital overlap at the junction. Furthermore, the twist angle and in-plane lattice displacement between flakes modify the interlayer coupling¹⁵⁶, ultimately breaking a single superconductivity order parameter into two.

One drawback of vertical JJs is the absence of gate tunability, which precludes the realization of gate-controlled qubits and quantum supercurrent transistors¹⁵⁷. However, the combination of hBN-encapsulated graphene heterostructures and 1D edge contacts to 2D layers¹³⁶ makes it possible to create a 2D electron gas in a highly homogeneous environment that is accessible laterally, with interfaces transparent for Cooper pairs. The large mean free path in this case allows ballistic transport in the lateral geometry, while the edge contacts eliminate the ill-defined travel distance of particles in Andreev reflections in devices with top contacts^{146,158,159}. In ballistic, graphene-based JJs, the gate voltage tunes the Fermi level and modifies the transmission probability of several conduction channels, resulting in tunable I_c (REFS^{159,160}). In addition, the current–phase relation $I(\varphi)$ shows deviations from a sinusoidal relation¹⁵⁸, while concurrently preserving a high I_c (REF.¹⁴⁶) up to $5 \mu\text{A } \mu\text{m}^{-1}$. Furthermore, deviations of I_c from the Fraunhofer pattern are expected when ballistic, graphene-based JJs are subjected to a magnetic field due to the large cyclotron orbit that breaks the Andreev electron–hole pairs¹⁴⁶. Nevertheless, a supercurrent^{161,162} is observed to survive in the quantum Hall regime (FIG. 4c), in which the ABSs circulate along the perimeter of the device. Although similar behaviour has been observed in JJs with 2D topological insulator (TI) weak links^{141,163}, the edge states in the TI case preserve time-reversal symmetry under zero magnetic field, such that they appear in pairs and carriers travel in both directions on each edge. By contrast, ballistic, graphene-based JJs in an applied magnetic field break time-reversal symmetry; thus, the edge states are chiral and carriers move in only one direction on each edge, but still support the supercurrent^{161,162}.

Recently, gate-tunable, ballistic, graphene-based JJs in a microwave circuit have been evaluated ($I_c R_N \approx 0.1 \Delta/e$), revealing microwave losses that are otherwise not accessible in DC measurements¹⁶⁴. These devices have been further integrated into gatemon qubits^{160,165}, in which temporal coherence and gate control of the qubit has been demonstrated¹⁶⁰ (FIG. 4d), yielding an energy relaxation time T_1 between 12 ns and 36 ns and a dephasing time T_2^* of ~ 55 ns (REF.¹⁶⁰). Although these times are relatively short, they represent a milestone for the integration of 2D materials in superconducting qubits and create opportunities for investigating 2D materials properties in a superconducting circuit. Graphene-based JJs may also find applications as single-photon detectors from visible to radio frequencies¹⁶⁶, which are essential for quantum key distribution. The proposed working principle is based on switching JJs from a zero-voltage state to a resistive state by Joule heating upon photon absorption. Although graphene has a desirably low electronic specific heat capacity due to the shrinking density of states at the charge-neutrality point, the challenge lies in achieving efficient light absorption, which could be potentially done by integrating plasmonic and/or optical cavity structures.

2D topological qubit platforms

Moving from conventional semiconductors with nearly free electrons to strongly correlated materials, we encounter strong interactions among particles and quasiparticles that produce exotic and intriguing phenomena with potential applications in quantum information science. For example, proposals for topological quantum computers are based on quasiparticles known as non-Abelian anyons that are described by topological quantum field theory. Indistinguishable particles in 3D space obey either Fermi–Dirac or Bose–Einstein statistics; in both cases, the interchange of two such particles leads to an additional phase term ($e^{i\theta} = \pm 1$) in the wave function ($\theta = 0$ for bosons and $\theta = \pi$ for fermions). In 2D, however, there are quasiparticles that are neither bosons nor fermions but anyons¹⁶⁷, and have the property that, when they are interchanged, the acquired phase can take values other than 0 or π ¹⁶⁸. The interchange also alters the ground state of the system if there is a degeneracy. After consecutive interchanges, the final state depends on the order of all the interchanges (that are non-commutative). These anyons are termed non-Abelian anyons because they obey non-Abelian statistics^{7,169}. An intuitive picture is that the trajectories of a group of non-Abelian anyons evolving in the 3D space–time braid together in a manner analogous to how knots are formed, such that the final state is only dependent on the topology of the braids and not on the specific geometry (FIG. 5a). Therefore, a topological qubit can be represented by the topological characteristics of the braids. Because smooth deformations of braids do not change their topological properties, these qubits are insensitive to local perturbations and, thus, ideal for fault-tolerant quantum computing¹⁷⁰.

A representative example of non-Abelian anyons are Majorana bound states (MBSs, also called Majorana zero modes, which are localized Majorana fermions¹⁷¹), which exist in a variety of systems, including those with triplet pairing, such as certain even-denominator,

fractional quantum Hall systems¹⁷². Unlike the conventional Hall effect, in which the Hall voltage increases linearly with the out-of-plane magnetic field, the quantum Hall voltage displays stepwise increases. At each step, the Hall conductance takes quantized values of $\nu e^2/h$, where ν takes integer and fractional values in the integer quantum Hall (IQH) and fractional quantum Hall effects (FQH), respectively. Whereas the IQH effect is a consequence of the Landau quantization of a 2D electron gas, multiple theories exist for the origin of the FQH effect. In the composite fermion approach¹⁷³, electrons bind with flux quanta to form new quasiparticles that have fractional elementary charge as a result of Coulomb interactions and strong correlations. The even-denominator $\nu = 5/2$ state is explained as the non-Abelian Moore–Read Pfaffian state¹⁷², in which the composite fermions have triplet pairing as in *p*-wave superconductors, which is especially attractive for quantum computing applications. A FQH effect with $\nu = 1/3$ was realized in 2D materials using high-mobility, suspended monolayer graphene^{174,175}. With the aid of hBN substrates and hBN encapsulation, the mobility of graphene was further improved, allowing additional FQH states to be observed in both monolayer^{176–179} and bilayer graphene^{180–182}. In particular, even-denominator states were observed in bilayer graphene¹⁸², consistent with the expected Pfaffian state¹⁸³ (FIG. 5b).

In addition to FQH systems, *p*-wave superconductors¹⁸⁴ and TI–superconductor hybrids^{185–189} have expanded the range of materials that host Majorana fermions. In *p*-wave superconductors, Cooper pairs have spin triplet pairing with an orbital angular momentum of \hbar . The Abrikosov vortices in these superconductors are promising candidates to host MBSs¹⁸⁴; $2N$ vortices give rise to 2^N -fold ground-state degeneracy¹⁸⁵. The challenges lie in the synthesis of *p*-wave superconductors, observation of vortices, detection of MBSs in the vortices and manipulation of the vortices (that is, braiding). Whereas the physical realization of an intrinsic *p*-wave superconductor has not yet been demonstrated (although triplet pairing has been theoretically proposed for Sr_2RuO_4 (REF.¹⁸⁴)), 2D heterostructures integrating *s*-wave superconductivity and spin-helical states (such as semiconductors with large Rashba spin–orbit coupling¹⁹⁰) realize a superconducting state resembling that of a *p*-wave superconductor^{169,185}. Proximity-induced superconductivity in TIs has been confirmed in transport measurement of JJs¹⁴¹, and the persistence of topological surface states has been verified in $\text{Bi}_2\text{Se}_3/\text{NbSe}_2$ heterostructures¹⁸⁶. To obtain an atomically sharp and electronically transparent interface, multi-quintuple-layer (QL) Bi_2Se_3 thin films (~ 1 nm per QL) have been grown by molecular beam epitaxy onto NbSe_2 substrates with the aid of bilayer $\text{Bi}(110)$ as a buffer layer¹⁸⁶. The extension of superconductivity to Bi_2Se_3 was revealed by the presence of superconductivity gaps in scanning tunnelling spectra, which weaken for thicker Bi_2Se_3 , whereas surface-state Dirac cones are preserved in 6-QL (and thicker) Bi_2Se_3 layers. Vortices arranged in a hexagonal pattern were subsequently observed in a similar system composed of $\text{Bi}_2\text{Te}_3/\text{NbSe}_2$ heterostructures¹⁸⁹ (also with a Bi bilayer at the interface)

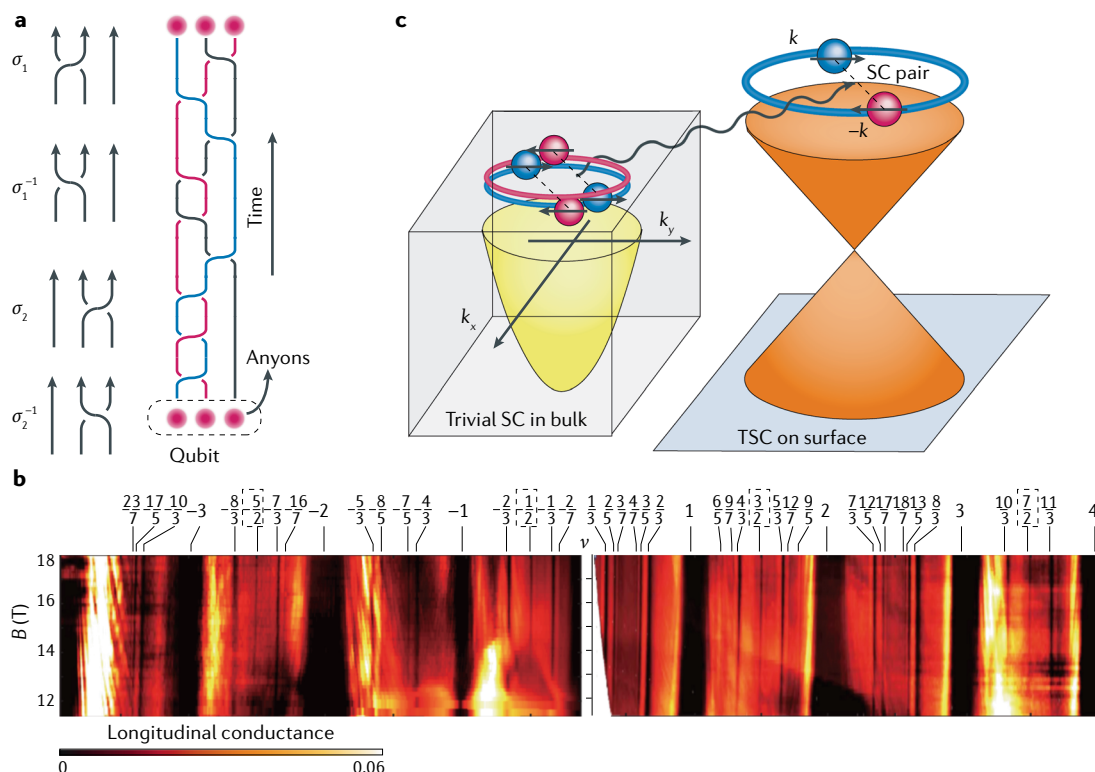


Fig. 5 | Topological quantum computing. **a** | Left: schematic representation of two braid operators (σ_1 and σ_2) and their inverses (σ_1^{-1} and σ_2^{-1}) for three-anyon braids. Right: an example of the evolution (braiding) of a three-anyon qubit. **b** | Longitudinal conductance of hexagonal boron nitride (hBN)-encapsulated bilayer graphene as a function of magnetic field B and filling factor ν . A number of fractional quantum Hall states are seen as conductance minima, including four even-denominator states (highlighted by the dashed lines). **c** | Schematic illustration of topologically non-trivial superconductivity induced in surface states with helical spin textures for layered $\text{FeTe}_{0.55}\text{Se}_{0.45}$. The yellow band is the bulk band, in which the s-wave superconducting pairing is topologically trivial. The orange band is the surface-state band; here, the electrons form superconducting pairs, owing to the bulk superconductivity, but because the surface states are topologically non-trivial, the superconducting state is also nontrivial. SC, superconductivity; TSC: topological SC. Panel **b** is adapted with permission from REF.¹⁸², AAAS. Panel **c** is adapted with permission from REF.¹⁹⁹, AAAS.

in a magnetic field. Vortex sizes in single-band s-wave superconductors are insensitive to small magnetic fields, whereas the vortex sizes in $\text{Bi}_2\text{Te}_3/\text{NbSe}_2$ decrease quickly with increasing field strength, likely a characteristic feature of a topological superconductor¹⁸⁹.

The spectroscopic signature of MBSs is a zero-energy peak in scanning tunnelling spectra (that is, a peak at the Fermi energy), which can be masked by other low-energy excitations, such as ABSs. However, the spatial distribution of MBSs in a vortex core may differ from that of other excitations, hinting at possible differentiation with spatially resolved spectroscopy. Indeed, splitting of the zero-energy peak in the vortex cores of $\text{Bi}_2\text{Te}_3/\text{NbSe}_2$ has been observed when moving at least 10 nm away from the vortex centre¹⁸⁷, in contrast to the zero-distance splitting present in NbSe_2 itself, which can be explained by the large spatial extent (~ 40 nm) of trapped Majorana fermions in vortex cores¹⁹¹. Furthermore, the magnetic-field dependence of the zero-energy peak resulting from MBSs and ABSs differ substantially¹⁸⁷, as the MBS peak height decreases sharply with increasing field strength. An additional spectroscopic signature of MBSs results from the predicted influence of Majorana fermions on the spin polarization of ABSs, implying that

reflected counterpropagating holes share the same spin polarization as incoming electrons¹⁹². This effect is manifested as a change in the zero-energy differential tunnelling conductance at a vortex core when the relative spin polarization between the STM tip and an external magnetic field is changed¹⁸⁸. Similar TI–superconductor heterostructures have been realized with other TIs, such as $\text{BiSbTe}_{1.25}\text{Se}_{1.75}$ (REF.¹⁹³) and few-layer Bi (REF.¹⁹⁴) in contact with NbSe_2 . Increasing evidence suggests the existence of MBSs in this type of systems, but effective control of doping levels in synthetic topological superconductors is critical. This requirement results from the need to realize an energy gap to stabilize a non-Abelian system by separating its degenerate ground states from its excitations¹⁶⁹. This gap is inversely proportional to the energy difference between the Dirac point of the topological surface state and the Fermi energy¹⁸⁹.

Iron-based superconductors are layered materials that have been grown and studied in the 2D limit on various substrates. Specifically, monolayer FeSe grown on SrTiO_3 is a model system for studying and engineering interfacial superconductivity, owing to its high T_c exceeding 100 K (REF.¹⁹⁵). FeSe has also attracted attention owing to its 1D topological edge states that coexist

with high- T_c superconductivity¹⁹⁶, making it a 2D material that uniquely supports both topological states and superconductivity. Meanwhile, a robust, zero-energy bound state has been detected¹⁹⁷ in scanning tunnelling spectroscopy measurements of interstitial Fe defects in $\text{FeTe}_{0.5}\text{Se}_{0.5}$ ($T_c = 12$ K), in which Te substitution introduces topological order with large spin–orbit coupling¹⁹⁸. The absence of Zeeman splitting in a magnetic field rules out that this peak is a Kondo resonance. A recent study has also suggested that $\text{FeTe}_{0.55}\text{Se}_{0.45}$ ($T_c = 14.5$ K) not only possesses Dirac-cone-type surface states but also a helical spin texture in its surface states, implying a non-trivial topology¹⁹⁹ (FIG. 5c). Below T_c , the bulk superconductivity opens an s -wave gap in the surface states, revealing the topological nature of superconductivity, which has been further corroborated by the observation of zero-energy peaks in scanning tunnelling spectra at vortex cores²⁰⁰. Because magnetic clusters or domains locally suppress superconductivity, itinerant Majorana modes may circulate around domain edges, which could explain the zero-energy peak observed at Fe defects¹⁹⁷. It should be noted that discrete Caroli–de Gennes–Matricon states also exist at energies close to zero in a vortex core; thus, an energy resolution well below 1 meV is required to identify a true zero-energy peak^{201–203}. In addition to Majorana fermions, parafermions (another type of non-Abelian anyon) have also been predicted to be suitable for topological quantum computing²⁰⁴, but have not yet been detected. Moreover, limited testing has been performed to confirm the non-Abelian statistics in these non-Abelian anyon systems.

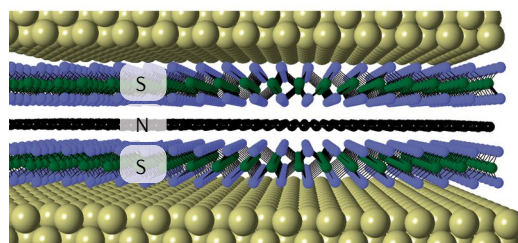
Conclusions and outlook

We have reviewed the four primary opportunities for 2D materials in quantum information sciences: quantum-dot qubits, single-photon emitters, superconducting qubits and topological quantum computing platforms. The main advantage offered by 2D materials is their diverse range of materials properties (they include Dirac¹⁷⁶ and Weyl²⁰⁵ semimetals, TIs²⁰⁶ and superconductors²⁰⁷) that enable the fabrication of novel heterostructures with functionalities unavailable in bulk crystals. In addition, many synthetic strategies, including growth and assembly schemes with wafer-scale homogeneity¹³⁷ and tunability over interfaces and defects^{9,72}, have been well developed. With the recent development of synthetic 2D materials (that is, 2D materials that do not have a bulk counterpart and cannot be obtained via exfoliation, such as borophene^{208–210} and stanene²¹¹), the range of 2D building blocks will also continue to grow. However, despite significant advances in 2D material synthesis, handling and characterization, 2D quantum information technologies are far from mature, and major challenges remain for scaling up qubit circuits and realizing coordinated quantum computation.

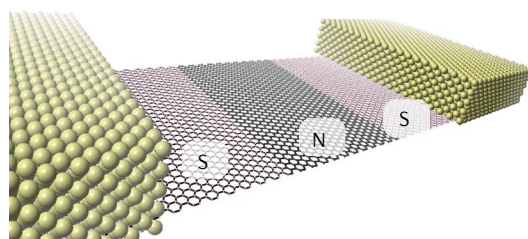
Heterostructures. The atomically abrupt and clean interfaces obtained in 2D heterostructures lie at the heart of realizations of quantum phenomena and quantum devices. For example, it would be highly advantageous to fabricate JJs using 2D vertical heterostructures via bottom-up van der Waals epitaxy (FIG. 6a), because the resulting atomically well-defined interfaces and high

a Bottom-up heterostructures

2D vertical heterostructures

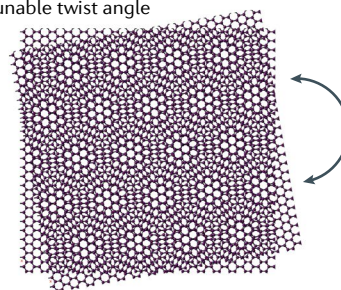


2D lateral heterostructures



b Controlled fabrication

Tunable twist angle



Creation of single-photon emitters

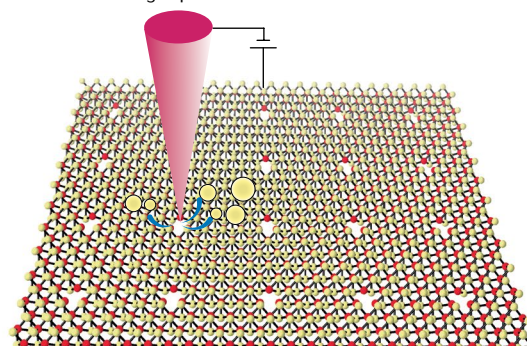


Fig. 6 | **Emerging opportunities.** **a** | Fabrication of Josephson junctions with 2D vertical (top) and 2D lateral (bottom) heterostructures from bottom-up growth results in atomically sharp and pristine interfaces. **b** | Schematic representation of continuous tuning of the twist angle between two monolayers (top). Creation of arrays of atomically well-defined single-photon emitters by scanning probe nanolithography at the atomic scale (bottom). N, normal or weak link; S, superconducting.

crystal quality would result in lower loss and, thus, improved coherence. Even more challenging is the direct growth of 2D lateral heterostructures (FIG. 6a), in which lattice-matching constraints play a significantly greater role than 2D vertical van der Waals heterostructures. If successful, the resulting 1D superconducting–normal interfaces would represent the ultimate form of edge contact; this has been attempted in graphene-based JJs but not yet realized with atomically well-defined and abrupt interfaces. The planar geometry of 2D lateral heterojunctions would also facilitate spatially resolved characterization with methods such as scanning probe microscopy, which would improve mechanistic understanding and accelerate technological development.

Interfacial engineering⁹ in 2D heterostructures may also present new opportunities for tailoring interfacial superconductivity. For example, by interfacing monolayer FeSe with different 2D materials, interfacial charge transfer and electron–phonon coupling, which are known to contribute to the high T_c of FeSe on SrTiO₃ (REF.¹⁹⁵), can be modulated. The combination of quantum anomalous Hall (QAH) insulators with *s*-wave superconductors is another potential platform for topological quantum computing²¹². Initial realizations of the QAH effect have been obtained through magnetic doping of layered TIs (such as Cr-doped (Bi_xSb_{1-x})₂Te₃)²¹³, which has limited the observation temperature to ultra-low temperatures (below 4 K), due to the electronic and mass-gap disorder induced by random dopants. Alternatively, by fabricating vertical heterostructures of a TI on top of a ferromagnetic insulator with atomically precise interfaces, the interfacial exchange coupling may be strong enough to induce a sizable mass gap with minimal disorder, thus facilitating higher-temperature observation and utilization of the QAH effect. Notably, MnBi₂Te₄, which is a van der Waals crystal composed of Bi₂Te₃ QIs and MnTe bilayers, has been recently demonstrated to be an intrinsic magnetic TI with bulk antiferromagnetism and minimal chemical disorder, allowing the observation of the QAH effect at 4.5 K (REFS^{214–217}).

Advanced fabrication techniques. Although superlattice devices based on graphene bilayers and graphene/hBN heterostructures have been extensively studied, a recent surge in activity in so-called twistrionics (that is, the study of effects arising in stacks of 2D materials twisted with respect to one another) has emerged after the observation of Mott-insulating phases²¹⁸ and unconventional superconductivity²¹⁹ in magic-angle bilayer graphene. The high sensitivity of the system properties on twist angles down to a fraction of a degree calls for more robust, universal and efficient techniques for controlling twist angles. In particular, a continuously tunable twist angle would expedite the exploration of phase transitions and, potentially, of other emergent phenomena that could fundamentally inform the field of quantum information sciences (FIG. 6b). An atomic force microscopy tip can be used to twist thick hBN structures²²⁰, but the ability to controllably twist monolayer materials is highly demanded. The use of scanning probe nanolithography²²¹ may also facilitate the creation of atomically well-defined SPEs in 2D materials by locally inducing defects (FIG. 6b), although more scalable methods with nanometre-scale precision will ultimately be needed for widely deployed quantum technologies. In addition, because many of the most recent entries to the 2D materials family (such as black phosphorus^{222,223}, InSe (REF.²²⁴) and CrI₃ (REF.²²⁵)) have the added challenge that they are highly reactive²²⁶ when exposed to ambient conditions and standard solvents, a substantial effort will be required to develop fabrication, processing and encapsulation schemes that will allow the preservation of the underlying materials properties in fully integrated quantum devices and systems. Consequently, the realization of quantum information technology will ultimately require multidisciplinary contributions from physicists, electrical engineers and computer scientists, but the underlying foundation will remain the base materials, in which key innovations are still required from materials scientists and engineers.

Published online 19 August 2019

- Feynman, R. P. Simulating physics with computers. *Int. J. Theor. Phys.* **21**, 467–488 (1982).
- Shor, P. W. Polynomial-time algorithms for prime factorization and discrete logarithms on a quantum computer. *SIAM J. Comput.* **26**, 1484–1509 (1997).
- DiVincenzo, D. P. The physical implementation of quantum computation. *Fortschr. Phys.* **48**, 771–783 (2000).
- Vandersypen, L. M. K. et al. Experimental realization of Shor's quantum factoring algorithm using nuclear magnetic resonance. *Nature* **414**, 883–887 (2001).
- Monz, T. et al. Realization of a scalable Shor algorithm. *Science* **351**, 1068–1070 (2016).
- Novoselov, K. S. et al. Two-dimensional gas of massless Dirac fermions in graphene. *Nature* **438**, 197 (2005).
- Nayak, C., Simon, S. H., Stern, A., Freedman, M. & Das Sarma, S. Non-Abelian anyons and topological quantum computation. *Rev. Mod. Phys.* **80**, 1083–1159 (2008).
- Qian, X., Liu, J., Fu, L. & Li, J. Quantum spin Hall effect in two-dimensional transition metal dichalcogenides. *Science* **346**, 1344–1347 (2014).
- Liu, X. & Hersam, M. C. Interface characterization and control of 2D materials and heterostructures. *Adv. Mater.* **30**, 1801586 (2018).
- Hanson, R., Kouwenhoven, L. P., Petta, J. R., Tarucha, S. & Vandersypen, L. M. K. Spins in few-electron quantum dots. *Rev. Mod. Phys.* **79**, 1217–1265 (2007).
- Loss, D. & DiVincenzo, D. P. Quantum computation with quantum dots. *Phys. Rev. A* **57**, 120–126 (1998).
- Nowack, K. C., Koppens, F. H. L., Nazarov, Y. V. & Vandersypen, L. M. K. Coherent control of a single electron spin with electric fields. *Science* **318**, 1430–1433 (2007).
- Rashba, E. I. & Efros, A. L. Orbital mechanisms of electron-spin manipulation by an electric field. *Phys. Rev. Lett.* **91**, 126405 (2003).
- Pioro-Ladrière, M. et al. Electrically driven single-electron spin resonance in a slanting Zeeman field. *Nat. Phys.* **4**, 776–779 (2008).
- Koppens, F. H. L. et al. Driven coherent oscillations of a single electron spin in a quantum dot. *Nature* **442**, 766–771 (2006).
- Kloeffel, C. & Loss, D. Prospects for spin-based quantum computing in quantum dots. *Annu. Rev. Condens. Matter Phys.* **4**, 51–81 (2013).
- Medford, J. et al. Quantum-dot-based resonant exchange qubit. *Phys. Rev. Lett.* **111**, 050501 (2013).
- Landig, A. J. et al. Coherent spin–photon coupling using a resonant exchange qubit. *Nature* **560**, 179–184 (2018).
- Gorman, J., Hasko, D. G. & Williams, D. A. Charge-qubit operation of an isolated double quantum dot. *Phys. Rev. Lett.* **95**, 090502 (2005).
- Hayashi, T., Fujisawa, T., Cheong, H. D., Jeong, Y. H. & Hirayama, Y. Coherent manipulation of electronic states in a double quantum dot. *Phys. Rev. Lett.* **91**, 226804 (2003).
- Nadj-Perge, S., Frolov, S. M., Bakkers, E. P. A. M. & Kouwenhoven, L. P. Spin–orbit qubit in a semiconductor nanowire. *Nature* **468**, 1084–1087 (2010).
- Stockklauser, A. et al. Strong coupling cavity QED with gate-defined double quantum dots enabled by a high impedance resonator. *Phys. Rev. X* **7**, 011030 (2017).
- Mi, X., Cady, J. V., Zajac, D. M., Deelman, P. W. & Petta, J. R. Strong coupling of a single electron in silicon to a microwave photon. *Science* **355**, 156–158 (2017).
- Samkharadze, N. et al. Strong spin-photon coupling in silicon. *Science* **359**, 1123–1127 (2018).
- De Sousa, R. & Sarma, S. D. Electron spin coherence in semiconductors: Considerations for a spin-based solid-state quantum computer architecture. *Phys. Rev. B* **67**, 033301 (2003).
- Fuchs, M., Rychkov, V. & Trauzettel, B. Spin decoherence in graphene quantum dots due to hyperfine interaction. *Phys. Rev. B* **86**, 085301 (2012).
- Huertas-Hernando, D., Guinea, F. & Brataas, A. Spin-orbit coupling in curved graphene, fullerenes, nanotubes, and nanotube caps. *Phys. Rev. B* **74**, 155426 (2006).
- Güttlinger, J., Frey, T., Stampfer, C., Ihn, T. & Ensslin, K. Spin states in graphene quantum dots. *Phys. Rev. Lett.* **105**, 116801 (2010).

29. Hanson, R. et al. Zeeman energy and spin relaxation in a one-electron quantum dot. *Phys. Rev. Lett.* **91**, 196802 (2003).
30. Eich, M. et al. Spin and valley states in gate-defined bilayer graphene quantum dots. *Phys. Rev. X* **8**, 031023 (2018).
31. Cho, C.-H., Kim, B.-H. & Park, S.-J. Room-temperature Coulomb blockade effect in silicon quantum dots in silicon nitride films. *Appl. Phys. Lett.* **89**, 013116 (2006).
32. Shin, S. J. et al. Room-temperature charge stability modulated by quantum effects in a nanoscale silicon island. *Nano Lett.* **11**, 1591–1597 (2011).
33. Ponomarenko, L. A. et al. Chaotic Dirac billiard in graphene quantum dots. *Science* **320**, 356–358 (2008).
34. Wurm, J. et al. Symmetry classes in graphene quantum dots: universal spectral statistics, weak localization, and conductance fluctuations. *Phys. Rev. Lett.* **102**, 056806 (2009).
35. Stampfer, C. et al. Energy gaps in etched graphene nanoribbons. *Phys. Rev. Lett.* **102**, 056403 (2009).
36. Stampfer, C. et al. Tunable graphene single electron transistor. *Nano Lett.* **8**, 2378–2383 (2008).
37. Güttinger, J. et al. Electron-hole crossover in graphene quantum dots. *Phys. Rev. Lett.* **103**, 046810 (2009).
38. Volk, C. et al. Probing relaxation times in graphene quantum dots. *Nat. Commun.* **4**, 1753 (2013).
39. Schnez, S. et al. Observation of excited states in a graphene quantum dot. *Appl. Phys. Lett.* **94**, 012107 (2009).
40. Liu, X. L., Hug, D. & Vandersypen, L. M. K. Gate-defined graphene double quantum dot and excited state spectroscopy. *Nano Lett.* **10**, 1623–1627 (2010).
41. Fujisawa, T., Tokura, Y. & Hirayama, Y. Energy relaxation process in a quantum dot studied by DC current and pulse-excited current measurements. *Phys. B Condens. Matter* **298**, 573–579 (2001).
42. Engels, S. et al. Etched graphene quantum dots on hexagonal boron nitride. *Appl. Phys. Lett.* **103**, 073113 (2013).
43. Xue, J. et al. Scanning tunnelling microscopy and spectroscopy of ultra-flat graphene on hexagonal boron nitride. *Nat. Mater.* **10**, 282–285 (2011).
44. Katsnelson, M. I., Novoselov, K. S. & Geim, A. K. Chiral tunnelling and the Klein paradox in graphene. *Nat. Phys.* **2**, 620–625 (2006).
45. Matulis, A. & Peeters, F. M. Quasibound states of quantum dots in single and bilayer graphene. *Phys. Rev. B* **77**, 115423 (2008).
46. Bardarson, J. H., Titov, M. & Brouwer, P. W. Electrostatic confinement of electrons in an integrable graphene quantum dot. *Phys. Rev. Lett.* **102**, 226803 (2009).
47. Ohta, T., Bostwick, A., Seyller, T., Horn, K. & Rotenberg, E. Controlling the electronic structure of bilayer graphene. *Science* **313**, 951–954 (2006).
48. Oostinga, J. B., Heersche, H. B., Liu, X., Morpurgo, A. F. & Vandersypen, L. M. K. Gate-induced insulating state in bilayer graphene devices. *Nat. Mater.* **7**, 151–157 (2008).
49. Zhang, Y. et al. Direct observation of a widely tunable bandgap in bilayer graphene. *Nature* **459**, 820–823 (2009).
50. Alden, J. S. et al. Strain solitons and topological defects in bilayer graphene. *Proc. Natl. Acad. Sci. USA* **110**, 11256–11260 (2013).
51. Ju, L. et al. Topological valley transport at bilayer graphene domain walls. *Nature* **520**, 650–655 (2015).
52. Eich, M. et al. Coupled quantum dots in bilayer graphene. *Nano Lett.* **18**, 5042–5048 (2018).
53. Goossens, A. et al. Gate-defined confinement in bilayer graphene-hexagonal boron nitride hybrid devices. *Nano Lett.* **12**, 4656–4660 (2012).
54. Kurzmann, A. et al. Excited states in bilayer graphene quantum dots. *arXiv:1904.07185 [cond-mat.mes-hall]* (2019).
55. Klimov, N. N. et al. Electromechanical properties of graphene drumheads. *Science* **336**, 1557–1561 (2012).
56. Freitag, N. M. et al. Large tunable valley splitting in edge-free graphene quantum dots on boron nitride. *Nat. Nanotechnol.* **13**, 392–397 (2018).
57. Eng, K. et al. Isotopically enhanced triple-quantum-dot qubit. *Sci. Adv.* **1**, e1500214 (2015).
58. Connolly, M. R. et al. Gigahertz quantized charge pumping in graphene quantum dots. *Nat. Nanotechnol.* **8**, 417–420 (2013).
59. Volk, C. et al. Electronic excited states in bilayer graphene double quantum dots. *Nano Lett.* **11**, 3581–3586 (2011).
60. Chiu, K. L. et al. Magnetic-field-induced charge redistribution in disordered graphene double quantum dots. *Phys. Rev. B* **92**, 155408 (2015).
61. Rohling, N. & Burkard, G. Universal quantum computing with spin and valley states. *New J. Phys.* **14**, 083008 (2012).
62. Recher, P., Nilsson, J., Burkard, G. & Trauzettel, B. Bound states and magnetic field induced valley splitting in gate-tunable graphene quantum dots. *Phys. Rev. B* **79**, 085407 (2009).
63. Pereira, J. M., Peeters, F. M., Vasilopoulos, P., Costa Filho, R. N. & Farias, G. A. Landau levels in graphene bilayer quantum dots. *Phys. Rev. B* **79**, 195403 (2009).
64. Trauzettel, B., Bulaev, D. V., Loss, D. & Burkard, G. Spin qubits in graphene quantum dots. *Nat. Phys.* **3**, 192–196 (2007).
65. Fal'ko, V. Quantum information on chicken wire. *Nat. Phys.* **3**, 151–152 (2007).
66. Goldhaber-Gordon, D. et al. Kondo effect in a single-electron transistor. *Nature* **391**, 156–159 (1998).
67. Weinmann, D., Häusler, W. & Kramer, B. Spin blockades in linear and nonlinear transport through quantum dots. *Phys. Rev. Lett.* **74**, 984–987 (1995).
68. Sols, F., Guinea, F. & Neto, A. H. C. Coulomb blockade in graphene nanoribbons. *Phys. Rev. Lett.* **99**, 166803 (2007).
69. Deng, G.-W. et al. Charge number dependence of the dephasing rates of a graphene double quantum dot in a circuit QED architecture. *Phys. Rev. Lett.* **115**, 126804 (2015).
70. Deng, G.-W. et al. Coupling two distant double quantum dots with a microwave resonator. *Nano Lett.* **15**, 6620–6625 (2015).
71. Hamer, M. et al. Gate-defined quantum confinement in InSe-based van der Waals heterostructures. *Nano Lett.* **18**, 3950–3955 (2018).
72. Liu, X. et al. Rotationally commensurate growth of MoS₂ on epitaxial graphene. *ACS Nano* **10**, 1067–1075 (2016).
73. Manzeli, S., Ovchinnikov, D., Pasquier, D., Yazyev, O. V. & Kis, A. 2D transition metal dichalcogenides. *Nat. Rev. Mater.* **2**, 17033 (2017).
74. Schaibley, J. R. et al. Valleytronics in 2D materials. *Nat. Rev. Mater.* **1**, 16055 (2016).
75. Mak, K. F. & Shan, J. Photonics and optoelectronics of 2D semiconductor transition metal dichalcogenides. *Nat. Photonics* **10**, 216–226 (2016).
76. Toda, Y., Moriwaki, O., Nishioka, M. & Arakawa, Y. Efficient carrier relaxation mechanism in InGaAs/GaAs self-assembled quantum dots based on the existence of continuum states. *Phys. Rev. Lett.* **82**, 4114–4117 (1999).
77. Elzerman, J. M. et al. Few-electron quantum dot circuit with integrated charge read out. *Phys. Rev. B* **67**, 161308 (2003).
78. Björk, M. T. et al. Few-electron quantum dots in nanowires. *Nano Lett.* **4**, 1621–1625 (2004).
79. Kormányos, A., Zolyomi, V., Drummond, N. D. & Burkard, G. Spin-orbit coupling, quantum dots, and qubits in monolayer transition metal dichalcogenides. *Phys. Rev. X* **4**, 011034 (2014).
80. Pawłowski, J., Zebrowski, D. & Bednarek, S. Valley qubit in a gated MoS₂ monolayer quantum dot. *Phys. Rev. B* **97**, 155412 (2018).
81. Széchenyi, G., Chirilă, L. & Pályi, A. Impurity-assisted electric control of spin-valley qubits in monolayer MoS₂. *2D Mater.* **5**, 035004 (2018).
82. Lee, K., Kulkarni, G. & Zhong, Z. Coulomb blockade in monolayer MoS₂ single electron transistor. *Nanoscale* **8**, 7755–7760 (2016).
83. Song, X.-X. et al. Temperature dependence of Coulomb oscillations in a few-layer two-dimensional WS₂ quantum dot. *Sci. Rep.* **5**, 16113 (2015).
84. Song, X.-X. et al. A gate defined quantum dot on the two-dimensional transition metal dichalcogenide semiconductor WSe₂. *Nanoscale* **7**, 16867–16873 (2015).
85. Pisoni, R. et al. Gate-tunable quantum dot in a high quality single layer MoS₂ van der Waals heterostructure. *Appl. Phys. Lett.* **112**, 123101 (2018).
86. Wang, K. et al. Electrical control of charged carriers and excitons in atomically thin materials. *Nat. Nanotechnol.* **13**, 128–132 (2018).
87. Kane, B. E. A silicon-based nuclear spin quantum computer. *Nature* **393**, 133–137 (1998).
88. Pla, J. J. et al. A single-atom electron spin qubit in silicon. *Nature* **489**, 541–545 (2012).
89. Hill, C. D. et al. A surface code quantum computer in silicon. *Sci. Adv.* **1**, e1500707 (2015).
90. Abadillo-Uribe, J. C., Koiller, B. & Calderón, M. J. Two-dimensional semiconductors pave the way towards dopant-based quantum computing. *Beilstein J. Nanotechnol.* **9**, 2668–2673 (2018).
91. Exarhos, A. L., Hopper, D. A., Patel, R. N., Doherty, M. W. & Bassett, L. C. Magnetic-field-dependent quantum emission in hexagonal boron nitride at room temperature. *Nat. Commun.* **10**, 222 (2019).
92. Grosso, G. et al. Tunable and high-purity room temperature single-photon emission from atomic defects in hexagonal boron nitride. *Nat. Commun.* **8**, 705 (2017).
93. Tran, T. T., Bray, K., Ford, M. J., Toth, M. & Aharonovich, I. Quantum emission from hexagonal boron nitride monolayers. *Nat. Nanotechnol.* **11**, 37–41 (2016).
94. Moody, G. et al. Microsecond valley lifetime of defect-bound excitons in monolayer WSe₂. *Phys. Rev. Lett.* **121**, 057403 (2018).
95. Chakraborty, C., Kinnischtzke, L., Goodfellow, K. M., Beams, R. & Vamivakas, A. N. Voltage-controlled quantum light from an atomically thin semiconductor. *Nat. Nanotechnol.* **10**, 507–511 (2015).
96. Kok, P. et al. Linear optical quantum computing with photonic qubits. *Rev. Mod. Phys.* **79**, 135–174 (2007).
97. Dobrovitski, V. V., Fuchs, G. D., Falk, A. L., Santori, C. & Awschalom, D. D. Quantum control over single spins in diamond. *Annu. Rev. Condens. Matter Phys.* **4**, 23–50 (2013).
98. Maurer, P. C. et al. Room-temperature quantum bit memory exceeding one second. *Science* **336**, 1283–1286 (2012).
99. Neumann, P. et al. High-precision nanoscale temperature sensing using single defects in diamond. *Nano Lett.* **13**, 2738–2742 (2013).
100. Gupta, S., Yang, J.-H. & Yakobson, B. I. Two-level quantum systems in two-dimensional materials for single photon emission. *Nano Lett.* **19**, 408–414 (2019).
101. Toth, M. & Aharonovich, I. Single photon sources in atomically thin materials. *Annu. Rev. Phys. Chem.* **70**, 123–142 (2019).
102. Cassabois, G., Valvin, P. & Gil, B. Hexagonal boron nitride is an indirect bandgap semiconductor. *Nat. Photonics* **10**, 262–266 (2016).
103. Zhao, H.-Q., Fujiwara, M. & Takeuchi, S. Suppression of fluorescence phonon sideband from nitrogen vacancy centers in diamond nanocrystals by substrate effect. *Opt. Express* **20**, 15628–15635 (2012).
104. Li, X. et al. Nonmagnetic quantum emitters in boron nitride with ultranarrow and sideband-free emission spectra. *ACS Nano* **11**, 6652–6660 (2017).
105. Lounis, B. & Orrit, M. Single-photon sources. *Rep. Prog. Phys.* **68**, 1129–1179 (2005).
106. Jungwirth, N. R. et al. Temperature dependence of wavelength selectable zero-phonon emission from single defects in hexagonal boron nitride. *Nano Lett.* **16**, 6052–6057 (2016).
107. Huxter, V. M., Oliver, T. A. A., Budker, D. & Fleming, G. R. Vibrational and electronic dynamics of nitrogen-vacancy centres in diamond revealed by two-dimensional ultrafast spectroscopy. *Nat. Phys.* **9**, 744–749 (2013).
108. Tawfik, S. A. et al. First-principles investigation of quantum emission from hBN defects. *Nanoscale* **9**, 13575–13582 (2017).
109. Noh, G. et al. Stark tuning of single-photon emitters in hexagonal boron nitride. *Nano Lett.* **18**, 4710–4715 (2018).
110. Tran, T. T. et al. Robust multicolor single photon emission from point defects in hexagonal boron nitride. *ACS Nano* **10**, 7331–7338 (2016).
111. Ziegler, J. et al. Deterministic quantum emitter formation in hexagonal boron nitride via controlled edge creation. *Nano Lett.* **19**, 2121–2127 (2019).
112. Mendelson, N. et al. Engineering and tuning of quantum emitters in few-layer hexagonal boron nitride. *ACS Nano* **13**, 3132–3140 (2019).
113. Dai, Z., Liu, L. & Zhang, Z. Strain engineering of 2D materials: issues and opportunities at the interface. *Adv. Mater.* **0**, 1805417 (2019).
114. Ziegler, J. et al. Single-photon emitters in boron nitride nanococoons. *Nano Lett.* **18**, 2683–2688 (2018).
115. Srivastava, A. et al. Optically active quantum dots in monolayer WSe₂. *Nat. Nanotechnol.* **10**, 491–496 (2015).
116. Mak, K. F., He, K., Shan, J. & Heinz, T. F. Control of valley polarization in monolayer MoS₂ by optical helicity. *Nat. Nanotechnol.* **7**, 494–498 (2012).
117. He, Y.-M. et al. Single quantum emitters in monolayer semiconductors. *Nat. Nanotechnol.* **10**, 497–502 (2015).

118. Koperski, M. et al. Single photon emitters in exfoliated WSe_2 structures. *Nat. Nanotechnol.* **10**, 503–506 (2015).
119. Palacios-Berraquero, C. et al. Atomically thin quantum light-emitting diodes. *Nat. Commun.* **7**, 12978 (2016).
120. Wang, G. et al. Valley dynamics probed through charged and neutral exciton emission in monolayer WSe_2 . *Phys. Rev. B* **90**, 075413 (2014).
121. Kumar, S. et al. Resonant laser spectroscopy of localized excitons in monolayer WSe_2 . *Optica* **3**, 882–886 (2016).
122. Branny, A. et al. Discrete quantum dot like emitters in monolayer MoSe_2 : Spatial mapping, magneto-optics, and charge tuning. *Appl. Phys. Lett.* **108**, 142101 (2016).
123. Liu, X., Balla, I., Bergeron, H. & Hersam, M. C. Point defects and grain boundaries in rotationally commensurate MoS_2 on epitaxial graphene. *J. Phys. Chem. C* **120**, 20798–20805 (2016).
124. Peng, J.-P. et al. Molecular beam epitaxy growth and scanning tunneling microscopy study of TiSe_2 ultrathin films. *Phys. Rev. B* **91**, 121113 (2015).
125. KC, S., Longo, R. C., Addou, R., Wallace, R. M. & Cho, K. Impact of intrinsic atomic defects on the electronic structure of MoS_2 monolayers. *Nanotechnol.* **25**, 375703 (2014).
126. Hildebrand, B. et al. Doping nature of native defects in 1T-TiSe_2 . *Phys. Rev. Lett.* **112**, 197001 (2014).
127. Hong, J. et al. Exploring atomic defects in molybdenum disulfide monolayers. *Nat. Commun.* **6**, 6293 (2015).
128. Noh, J.-Y., Kim, H. & Kim, Y.-S. Stability and electronic structures of native defects in single-layer MoS_2 . *Phys. Rev. B* **89**, 205417 (2014).
129. Clark, G. et al. Single defect light-emitting diode in a van der Waals heterostructure. *Nano Lett.* **16**, 3944–3948 (2016).
130. Li, H. et al. Optoelectronic crystal of artificial atoms in strain-textured molybdenum disulfide. *Nat. Commun.* **6**, 7381 (2015).
131. Feng, J., Qian, X., Huang, C.-W. & Li, J. Strain-engineered artificial atom as a broad-spectrum solar energy funnel. *Nat. Photonics* **6**, 866–872 (2012).
132. Branny, A., Kumar, S., Proux, R. & Gerardot, B. D. Deterministic strain-induced arrays of quantum emitters in a two-dimensional semiconductor. *Nat. Commun.* **8**, 15053 (2017).
133. Palacios-Berraquero, C. et al. Large-scale quantum-emitter arrays in atomically thin semiconductors. *Nat. Commun.* **8**, 15093 (2017).
134. Rosenberger, M. R. et al. Quantum calligraphy: Writing single-photon emitters in a two-dimensional materials platform. *ACS Nano* **13**, 904–912 (2019).
135. Martinis, J. M. et al. Decoherence in Josephson qubits from dielectric loss. *Phys. Rev. Lett.* **95**, 210503 (2005).
136. Wang, L. et al. One-dimensional electrical contact to a two-dimensional material. *Science* **342**, 614–617 (2013).
137. Kang, K. et al. Layer-by-layer assembly of two-dimensional materials into wafer-scale heterostructures. *Nature* **550**, 229–233 (2017).
138. Makhlin, Y., Schön, G. & Shnirman, A. Quantum-state engineering with Josephson-junction devices. *Rev. Mod. Phys.* **73**, 357–400 (2001).
139. Scherer, H. & Camarota, B. Quantum metrology triangle experiments: a status review. *Meas. Sci. Technol.* **23**, 124010 (2012).
140. Likharev, K. K. Superconducting weak links. *Rev. Mod. Phys.* **51**, 101–159 (1979).
141. Williams, J. R. et al. Unconventional Josephson effect in hybrid superconductor-topological insulator devices. *Phys. Rev. Lett.* **109**, 056803 (2012).
142. Koch, J. et al. Charge-insensitive qubit design derived from the Cooper pair box. *Phys. Rev. A* **76**, 042319 (2007).
143. Larsen, T. W. et al. Semiconductor-nanowire-based superconducting qubit. *Phys. Rev. Lett.* **115**, 127001 (2015).
144. Shim, Y.-P. & Tahan, C. Semiconductor-inspired design principles for superconducting quantum computing. *Nat. Commun.* **7**, 11059 (2016).
145. Casparis, L. et al. Superconducting gatemon qubit based on a proximitized two-dimensional electron gas. *Nat. Nanotechnol.* **13**, 915–919 (2018).
146. Ben Shalom, M. et al. Quantum oscillations of the critical current and high-field superconducting proximity in ballistic graphene. *Nat. Phys.* **12**, 318–322 (2016).
147. Heersche, H. B., Jarillo-Herrero, P., Oostinga, J. B., Vandersypen, L. M. K. & Morpurgo, A. F. Bipolar supercurrent in graphene. *Nature* **446**, 56–59 (2007).
148. Rickhaus, P., Weiss, M., Marot, L. & Schönenberger, C. Quantum Hall effect in graphene with superconducting electrodes. *Nano Lett.* **12**, 1942–1945 (2012).
149. Chen, J.-H. et al. Diffusive charge transport in graphene on SiO_2 . *Solid State Commun.* **149**, 1080–1086 (2009).
150. Mizuno, N., Nielsen, B. & Du, X. Ballistic-like supercurrent in suspended graphene Josephson weak links. *Nat. Commun.* **4**, 2716 (2013).
151. Lee, G.-H., Kim, S., Jhi, S.-H. & Lee, H.-J. Ultimately short ballistic vertical graphene Josephson junctions. *Nat. Commun.* **6**, 6181 (2015).
152. Island, J. O., Steele, G. A., Zant, H. S. J. van der & Castellanos-Gomez, A. Thickness dependent interlayer transport in vertical MoS_2 Josephson junctions. *2D Mater.* **3**, 031002 (2016).
153. Kim, M. et al. Strong proximity Josephson coupling in vertically stacked NbSe_2 -graphene- NbSe_2 van der Waals junctions. *Nano Lett.* **17**, 6125–6130 (2017).
154. Frindt, R. F. Superconductivity in ultrathin NbSe_2 layers. *Phys. Rev. Lett.* **28**, 299–301 (1972).
155. Yabuki, N. et al. Supercurrent in van der Waals Josephson junction. *Nat. Commun.* **7**, 10616 (2016).
156. Liu, K. et al. Evolution of interlayer coupling in twisted molybdenum disulfide bilayers. *Nat. Commun.* **5**, 4966 (2014).
157. Jarillo-Herrero, P., van Dam, J. A. & Kouwenhoven, L. P. Quantum supercurrent transistors in carbon nanotubes. *Nature* **439**, 953–956 (2006).
158. Nanda, G. et al. Current-phase relation of ballistic graphene Josephson junctions. *Nano Lett.* **17**, 3396–3401 (2017).
159. Calado, V. E. et al. Ballistic Josephson junctions in edge-contacted graphene. *Nat. Nanotechnol.* **10**, 761–764 (2015).
160. Wang, J. I.-J. et al. Coherent control of a hybrid superconducting circuit made with graphene-based van der Waals heterostructures. *Nat. Nanotechnol.* **14**, 120–125 (2019).
161. Lee, G.-H. et al. Inducing superconducting correlation in quantum Hall edge states. *Nat. Phys.* **13**, 693–698 (2017).
162. Amet, F. et al. Supercurrent in the quantum Hall regime. *Science* **352**, 966–969 (2016).
163. Pribiag, V. S. et al. Edge-mode superconductivity in a two-dimensional topological insulator. *Nat. Nanotechnol.* **10**, 593–597 (2015).
164. Schmidt, F. E., Jenkins, M. D., Watanabe, K., Taniguchi, T. & Steele, G. A. A ballistic graphene superconducting microwave circuit. *Nat. Commun.* **9**, 4069 (2018).
165. Kroll, J. G. et al. Magnetic field compatible circuit quantum electrodynamics with graphene Josephson junctions. *Nat. Commun.* **9**, 4615 (2018).
166. Walsh, E. D. et al. Graphene-based Josephson-junction single-photon detector. *Phys. Rev. Applied* **8**, 024022 (2017).
167. Wilczek, F. Quantum mechanics of fractional-spin particles. *Phys. Rev. Lett.* **49**, 957–959 (1982).
168. Leinaas, J. M. & Myrheim, J. On the theory of identical particles. *Nuovo Cim. B* **37**, 1–23 (1977).
169. Stern, A. Non-Abelian states of matter. *Nature* **464**, 187–193 (2010).
170. Kitaev, A. Yu. Fault-tolerant quantum computation by anyons. *Ann. Phys.* **303**, 2–30 (2003).
171. Teo, J. C. Y. & Kane, C. L. Majorana fermions and non-Abelian statistics in three dimensions. *Phys. Rev. Lett.* **104**, 046401 (2010).
172. Moore, G. & Read, N. Nonabelians in the fractional quantum hall effect. *Nucl. Phys. B* **360**, 362–396 (1991).
173. Jain, J. K. Composite-fermion approach for the fractional quantum Hall effect. *Phys. Rev. Lett.* **63**, 199–202 (1989).
174. Du, X., Skachko, I., Duerr, F., Luican, A. & Andrei, E. Y. Fractional quantum Hall effect and insulating phase of Dirac electrons in graphene. *Nature* **462**, 192–195 (2009).
175. Bolotin, K. I., Ghahari, F., Shulman, M. D., Stormer, H. L. & Kim, P. Observation of the fractional quantum Hall effect in graphene. *Nature* **462**, 196–199 (2009).
176. Feldman, B. E., Krauss, B., Smet, J. H. & Yacoby, A. Unconventional sequence of fractional quantum Hall states in suspended graphene. *Science* **337**, 1196–1199 (2012).
177. Wang, L. et al. Evidence for a fractional fractal quantum Hall effect in graphene superlattices. *Science* **350**, 1231–1234 (2015).
178. Kim, Y. et al. Even denominator fractional quantum Hall states in higher Landau levels of graphene. *Nat. Phys.* **15**, 154–158 (2019).
179. Zibrov, A. A. et al. Even-denominator fractional quantum Hall states at an isospin transition in monolayer graphene. *Nat. Phys.* **14**, 930–935 (2018).
180. Zibrov, A. A. et al. Tunable interacting composite fermion phases in a half-filled bilayer-graphene Landau level. *Nature* **549**, 360–364 (2017).
181. Sanchez-Yamagishi, J. D. et al. Helical edge states and fractional quantum Hall effect in a graphene electron-hole bilayer. *Nat. Nanotechnol.* **12**, 118–122 (2017).
182. Li, J. I. A. et al. Even-denominator fractional quantum Hall states in bilayer graphene. *Science* **358**, 648–652 (2017).
183. Lin, X., Du, R. & Xie, X. Recent experimental progress of fractional quantum Hall effect: 5/2 filling state and graphene. *Nat. Sci. Rev.* **1**, 564–579 (2014).
184. Das Sarma, S., Nayak, C. & Tewari, S. Proposal to stabilize and detect half-quantum vortices in strontium ruthenate thin films: Non-Abelian braiding statistics of vortices in a $p_x + ip_y$ superconductor. *Phys. Rev. B* **73**, 220502 (2006).
185. Fu, L. & Kane, C. L. Superconducting proximity effect and Majorana fermions at the surface of a topological insulator. *Phys. Rev. Lett.* **100**, 096407 (2008).
186. Wang, M.-X. et al. The coexistence of superconductivity and topological order in the Bi_2Se_3 thin films. *Science* **336**, 52–55 (2012).
187. Xu, J.-P. et al. Experimental detection of a Majorana mode in the core of a magnetic vortex inside a topological insulator-superconductor $\text{Bi}_2\text{Te}_3/\text{NbSe}_2$ heterostructure. *Phys. Rev. Lett.* **114**, 017001 (2015).
188. Sun, H.-H. et al. Majorana zero mode detected with spin selective Andreev reflection in the vortex of a topological superconductor. *Phys. Rev. Lett.* **116**, 257003 (2016).
189. Xu, J.-P. et al. Artificial topological superconductor by the proximity effect. *Phys. Rev. Lett.* **112**, 217001 (2014).
190. Lutchyn, R. M., Sau, J. D. & Das Sarma, S. Majorana fermions and a topological phase transition in semiconductor-superconductor heterostructures. *Phys. Rev. Lett.* **105**, 077001 (2010).
191. Chiu, C.-K., Gilbert, M. J. & Hughes, T. L. Vortex lines in topological insulator-superconductor heterostructures. *Phys. Rev. B* **84**, 144507 (2011).
192. He, J. J., Ng, T. K., Lee, P. A. & Law, K. T. Selective equal-spin Andreev reflections induced by Majorana fermions. *Phys. Rev. Lett.* **112**, 037001 (2014).
193. Banerjee, A., Sundaresan, A., Ganesan, R. & Kumar, P. S. A. Signatures of topological superconductivity in bulk-insulating topological insulator $\text{BiSbTe}_{1-x}\text{Sb}_{2x}$ in proximity with superconducting NbSe_2 . *ACS Nano* **12**, 12665–12672 (2018).
194. Sun, H.-H. et al. Coexistence of topological edge state and superconductivity in bismuth ultrathin film. *Nano Lett.* **17**, 3035–3039 (2017).
195. Ge, J.-F. et al. Superconductivity above 100 K in single-layer FeSe films on doped SrTiO_3 . *Nat. Mater.* **14**, 285–289 (2015).
196. Wang, Z. F. et al. Topological edge states in a high-temperature superconductor $\text{FeSe}/\text{SrTiO}_3(001)$ film. *Nat. Mater.* **15**, 968–973 (2016).
197. Yin, J.-X. et al. Observation of a robust zero-energy bound state in iron-based superconductor $\text{Fe}(\text{Te},\text{Se})$. *Nat. Phys.* **11**, 543–546 (2015).
198. Xu, G., Lian, B., Tang, P., Qi, X.-L. & Zhang, S.-C. Topological superconductivity on the surface of Fe-based superconductors. *Phys. Rev. Lett.* **117**, 047001 (2016).
199. Zhang, P. et al. Observation of topological superconductivity on the surface of an iron-based superconductor. *Science* **360**, 182–186 (2018).
200. Wang, D. et al. Evidence for Majorana bound states in an iron-based superconductor. *Science* **362**, 333–335 (2018).
201. Machida, T. et al. Zero-energy vortex bound state in the superconducting topological surface state of $\text{Fe}(\text{Se},\text{Te})$. *Nat. Mater.* **18**, 811–881 (2019).
202. Chen, M. et al. Discrete energy levels of Caroli-de Gennes-Matricorn states in quantum limit in $\text{FeTe}_{0.55}\text{Se}_{0.45}$. *Nat. Commun.* **9**, 970 (2018).
203. Massee, F. et al. Imaging atomic-scale effects of high-energy ion irradiation on superconductivity and vortex pinning in $\text{Fe}(\text{Se},\text{Te})$. *Sci. Adv.* **1**, e1500033 (2015).
204. Clarke, D. J., Alicea, J. & Shtengel, K. Exotic non-Abelian anyons from conventional fractional quantum Hall states. *Nat. Commun.* **4**, 1348 (2013).
205. Li, P. et al. Evidence for topological type-II Weyl semimetal WTe_2 . *Nat. Commun.* **8**, 2150 (2017).
206. Wu, S. et al. Observation of the quantum spin Hall effect up to 100 kelvin in a monolayer crystal. *Science* **359**, 76–79 (2018).

207. Wang, H. et al. High-quality monolayer superconductor NbSe₂ grown by chemical vapour deposition. *Nat. Commun.* **8**, 394 (2017).
208. Mannix, A. J. et al. Synthesis of borophenes: Anisotropic, two-dimensional boron polymorphs. *Science* **350**, 1513–1516 (2015).
209. Liu, X., Zhang, Z., Wang, L., Yakobson, B. I. & Hersam, M. C. Intermixing and periodic self-assembly of borophene line defects. *Nat. Mater.* **17**, 783–788 (2018).
210. Liu, X. et al. Geometric imaging of borophene polymorphs with functionalized probes. *Nat. Commun.* **10**, 1642 (2019).
211. Zhu, F.-F. et al. Epitaxial growth of two-dimensional stanene. *Nat. Mater.* **14**, 1020–1025 (2015).
212. Lian, B., Sun, X.-Q., Vaezi, A., Qi, X.-L. & Zhang, S.-C. Topological quantum computation based on chiral Majorana fermions. *Proc. Natl. Acad. Sci. USA* **115**, 10938–10942 (2018).
213. Chang, C.-Z. et al. Experimental observation of the quantum anomalous Hall effect in a magnetic topological insulator. *Science* **340**, 167–170 (2013).
214. Yan Gong, J. G. & Yan Gong, J. G. Experimental realization of an intrinsic magnetic topological insulator. *Chin. Phys. Lett.* **36**, 076801 (2019).
215. Li, J. et al. Intrinsic magnetic topological insulators in van der Waals layered MnBi₂Te₄-family materials. *Sci. Adv.* **5**, eaaw5685 (2019).
216. Liu, C. et al. Quantum phase transition from axion insulator to Chern insulator in MnBi₂Te₄. *arXiv:1905.00715* [cond-mat.mes-hall] (2019).
217. Deng, Y. et al. Magnetic-field-induced quantized anomalous Hall effect in intrinsic magnetic topological insulator MnBi₂Te₄. *arXiv:1904.11468* [cond-mat.mtrl-sci] (2019).
218. Cao, Y. et al. Correlated insulator behaviour at half-filling in magic-angle graphene superlattices. *Nature* **556**, 80–84 (2018).
219. Cao, Y. et al. Unconventional superconductivity in magic-angle graphene superlattices. *Nature* **556**, 43–50 (2018).
220. Ribeiro-Palau, R. et al. Twistable electronics with dynamically rotatable heterostructures. *Science* **361**, 690–693 (2018).
221. Liu, X. et al. Scanning probe nanopatterning and layer-by-layer thinning of black phosphorus. *Adv. Mater.* **29**, 1604121 (2017).
222. Wood, J. D. et al. Effective passivation of exfoliated black phosphorus transistors against ambient degradation. *Nano Lett.* **14**, 6964–6970 (2014).
223. Ryder, C. R. et al. Covalent functionalization and passivation of exfoliated black phosphorus via aryl diazonium chemistry. *Nat. Chem.* **8**, 597–602 (2016).
224. Wells, S. A. et al. Suppressing ambient degradation of exfoliated InSe nanosheet devices via seeded atomic layer deposition encapsulation. *Nano Lett.* **18**, 7876–7882 (2018).
225. Shcherbakov, D. et al. Raman spectroscopy, photocatalytic degradation, and stabilization of atomically thin chromium tri-iodide. *Nano Lett.* **18**, 4214–4219 (2018).
226. Ryder, C. R., Wood, J. D., Wells, S. A. & Hersam, M. C. Chemically tailoring semiconducting two-dimensional transition metal dichalcogenides and black phosphorus. *ACS Nano* **10**, 3900–3917 (2016).

Acknowledgements

X.L. and M.C.H. acknowledge support from the Office of Naval Research (ONR N00014-17-1-2993) and the National Science Foundation Materials Research Science and Engineering Center (NSF DMR-1720139). X.L. further acknowledges support from a Ryan Fellowship that is administered through the Northwestern University International Institute for Nanotechnology.

Author contributions

X.L. researched the data for the article. All authors discussed the contents and provided important contributions to the manuscript.

Competing interests

The authors declare no competing interests.

Publisher's note

Springer Nature remains neutral with regard to jurisdictional claims in published maps and institutional affiliations.